

# Northumbria Research Link

Citation: Zharkova, Valentina, Zharkov, Sergei, Druett, Malcolm, Matthews, Sarah and Inoue, Satoshi (2020) Sunquake with a second bounce, other sunquakes, and emission associated with the X9.3 flare of 6 September 2017 - II. Proposed interpretation. *Astronomy & Astrophysics*, 639. A79. ISSN 0004-6361

Published by: EDP Sciences

URL: <https://doi.org/10.1051/0004-6361/202037885> <<https://doi.org/10.1051/0004-6361/202037885>>

This version was downloaded from Northumbria Research Link:  
<http://nrl.northumbria.ac.uk/id/eprint/43083/>

Northumbria University has developed Northumbria Research Link (NRL) to enable users to access the University's research output. Copyright © and moral rights for items on NRL are retained by the individual author(s) and/or other copyright owners. Single copies of full items can be reproduced, displayed or performed, and given to third parties in any format or medium for personal research or study, educational, or not-for-profit purposes without prior permission or charge, provided the authors, title and full bibliographic details are given, as well as a hyperlink and/or URL to the original metadata page. The content must not be changed in any way. Full items must not be sold commercially in any format or medium without formal permission of the copyright holder. The full policy is available online: <http://nrl.northumbria.ac.uk/policies.html>

This document may differ from the final, published version of the research and has been made available online in accordance with publisher policies. To read and/or cite from the published version of the research, please visit the publisher's website (a subscription may be required.)

# Sunquake with a second-bounce, other sunquakes and emission associated with X9.3 flare of 6 September 2017. II. Proposed interpretation

Valentina Zharkova<sup>1</sup>, Sergei Zharkov<sup>2</sup>, Malcolm Druett<sup>3</sup>, Sarah Matthews<sup>4</sup>, and Satoshi Inoue<sup>5</sup>

<sup>1</sup> Northumbria University, Department of Mathematics, Physics and Electrical Engineering, Newcastle upon Tyne, NE1 8ST, United Kingdom

<sup>2</sup> E.A.Milne Centre for Astrophysics, School of Mathematics and Physical Sciences, Hull University, Kingston upon Hull, HU6 7RX, United Kingdom

<sup>3</sup> Stockholm University, Department of Astronomy, SE-106 91 Stockholm, Sweden,

<sup>4</sup> UCL Mullard Space Science Laboratory, Holmbury St. Mary, Dorking, Surrey, RH5 6NT, United Kingdom

<sup>5</sup> Institute for Space–Earth Environmental Research (ISEE), Nagoya University, Furo-cho, Chikusa-ku, Nagoya, Japan, 464 8601

April 30, 2020

**Abstract.** In the paper 1 of this research we presented observations of the flare of 6 September 2017 in gamma-ray (GR), hard (HXR), soft X-rays (SXR), Ly $\alpha$  line, extra ultra-violet (EUV), H $\alpha$  and white light emission recorded during the two flaring events 1 (FE1) and 2 (FE2) occurred from 11:55:37 UT (FE1) and 12:06:40 UT (FE2). In paper 1 for the first time detection of the sunquake with two bounces of seismic waves was reported with observations of another four sunquakes observed simultaneously in HXR, GR, EUV, H $\alpha$  and white light emission with strongly varying spatial resolution and temporal coverage. In the current paper 2 we propose some likely scenarios of heating flaring atmospheres in the footpoints with sunquakes which were supported with EUV and H $\alpha$  emission. We use a range of parameters derived from the HXR, EUV and H $\alpha$  line observations to generate hydrodynamic models, which can account for the blue shifts derived from the EUV emission and the red shifts observed with EIS in He II line and by CRISP/SST in H $\alpha$  line emission. The parameters of hydrodynamic shocks produced by different beams in flaring atmospheres are used as the initial conditions for another type of hydrodynamic models developed for acoustic wave propagation in the solar interior to simulate the sets of acoustic waves produced in the solar interior by the hydrodynamic shocks deposited in different footpoints of magnetic loops. The interpretation of H $\alpha$  line profiles with large red shifts in three kernels (two in FE1 and one in FE2) was carried out by fitting spectral observations to the full NLTE radiative simulations in optically thick transitions (Lyman lines and continuum, H $\alpha$ , H $\beta$ , P $\alpha$ ) for flaring atmospheres with fast downward motion assuming non-thermal excitation and ionisation by energetic power-law electron beams. The largest sunquake (seismic source 2 in FE1) is found consistent with being induced by a strong hydrodynamic shock produced by a mixed beam deposited at an angle of  $-30^\circ$  from the local vertical. We explain the occurrence of a second bounce in the largest sunquake by a stronger momentum delivered by the shock generated in the atmosphere above by the mixed beam, which then was deposited under the angle allowing the acoustic waves to conserve enough energy for the second bounces from the interior layers and the photosphere. The wave characteristics of seismic sources 1 and 3 (in FE1) were consistent with those produced by the shocks generated by similar mixed beams deposited at the angles  $+0^\circ$  (seismic source 1) and  $+30^\circ$  (seismic source 3) to the local vertical. The differences of seismic signatures produced in the flares of 6 September 2011 and 2017 are also discussed.

**Key words.** Sun: flares, Sun: X-rays, gamma-rays, Sun: helioseismology, radiative transfer, hydrodynamics

## 1. Introduction

On the 6 September 2017 the active region NOAA 12673 produced two X-class flares: an X2.2 flare and three hours later an X9.3 flare that have been studied by many au-

thors. A few sunquakes and magneto-acoustic waves associated with the X9.3 flare were originally reported by Sharykin & Kosovichev (2018); Zhao & Chen (2018). The X9.3 flare of 6 September 2017 was explored in our paper, part 1 (Zharkov et al. 2020, thereafter paper 1) presenting the available observations of gamma-ray (GR), hard X-ray (HXR), extra ultra-violet (EUV), H $\alpha$  and white light emission combined with four (possibly five) sunquakes detected by the Helioseismic and Magnetic Imager (HMI) aboard Solar Dynamic Observatory (SDO) (Scherrer et al. 2012). In our first paper on this flare investigation (Zharkov et al. 2020, thereafter Paper 1) for the first

Send offprint requests to: v.zharkova e-mail: valentina.zharkova@northumbria.ac.uk



time we presented detection of the largest sunquake with the first and second bounces of acoustic waves generated in the solar interior. There were also another 3 (potentially 4) sunquakes detected with rather different characteristics. In the current paper 2 we compare the conditions in flaring atmospheres leading to sunquakes generated around given footpoints of magnetic loops restored with the non-linear force-free field (NLFFF) extrapolation of the magnetic field in this active region prior the flare onset followed by 3D MHD simulations of the magnetic structure which led to the flare of 6 September 2017 (Inoue et al. 2018).

The X9.3 flare was observed with the Gamma Ray Burst Detector (KONUS) payload (Lysenko et al. 2019) aboard WIND satellite (Aptekar et al. 1995), with Ly $\alpha$  light curves by the Large-Yield RAdiometer (LYRA) instrument on board of the PROBA 2 satellite (Hochedez et al. 2006; Dominique et al. 2013) showing four flaring events (FEs), from which we analysed FE1 and FE2 (see for details Zharkov et al. 2020). There were also observations with the Reuven Ramaty High Energy Solar Spectroscopic Imager (RHESSI) (Lin et al. 2002) occurred 1.2 minutes after FE2. Since neither the KONUS/WIND or LYRA data do have any spatial resolution and the HXR observations by RHESSI were not available for FE1 and FE2, thus, they cannot be used directly for the beam parameter definition. Hence, for this flare we are left with H $\alpha$  emission locations observed with the CRisp Imaging Spectro-Polarimeter (CRISP) (Scharmer et al. 2003; Scharmer 2006) at Swedish Solar Telescope (SST) to distinguish the areas of the footpoints where heating by the beams has occurred that can provide us with some guidance about a range of the parameters of particle beams generating these signatures.

The flaring atmosphere parameters were derived in Paper 1 (Zharkov et al. 2020) from the EUV observations with the EUV Imaging Spectrometer (EIS) on Hinode (Culhane et al. 2007) in the spectrograms for the Fe XXIII 263.76 Å line profiles for large blue shifts and He II 256 Å line profiles revealing red shifts during the impulsive phase followed later by the blue ones. For the dynamics of lower atmosphere in flaring events 1 and 2 we explored from H $\alpha$  line profile observations by the CRISP/SST instrument in two H $\alpha$  kernels for FE1 linked to seismic sources 1 and 2 and one H $\alpha$  kernel 3 in FE2 seen 10 minutes later in the same location as seismic source 2. The H $\alpha$  line profiles in each locations indicate the observation of blue wings of the profiles while the core being strongly red-shifted well beyond the spectral window of  $\pm 1.5\text{Å}$  for the CRISP/SST. Moreover, the SST observations in the available wavelength range are consistent with the previous observations of Hydrogen H $\alpha$  line emission, often revealing cores with large red shifts up to 5 Å (Ichimoto & Kurokawa 1984; Canfield & Gayley 1987; Zarro et al. 1988; Wuelser & Marti 1989).

In addition, there was an increase in white light (WL) (Paschen continuum) in this flare similarly to many other flaring events (Uchida & Hudson 1972; Kurokawa et al. 1988; Matthews et al. 2011) and Balmer continuum emission (Kotř et al. 2016), which are nearly co-spatial with the HXR emission. Uchida & Hudson (1972) suggested that a sharp increase of continuous emission in flares is caused by energetic electron beams injected into a flaring atmosphere. Recently, Druett

et al. (2017); Druett & Zharkova (2018) have shown that non-thermal ionisation of hydrogen atoms by relativistic electron beams can naturally produce strong increases in Balmer near UV and Paschen white light (WL) emission during flares at the chromospheric levels, in addition to photospheric depths while producing the profiles of H $\alpha$  lines strongly (by 3-5 Å) shifted to the red wings leaving only blue wings of the line for observations with a narrow spectral filter of  $\pm 1.5\text{Å}$ .

The high-energy emissions in HXR, EUV, UV and optical wavelengths are often accompanied by the occurrence of sunquakes, or ripples on the solar surface radially emanating from a point source from 20-30 minutes to up an hour after a flare onset (Kosovichev & Zharkova 1998; Zharkova 2008; Donea 2011; Zharkov et al. 2011a; Zharkov et al. 2011b; Matthews et al. 2015). Sunquakes are detected on the solar surface using time-distance (TD) diagram analysis (Kosovichev & Zharkova 1998; Zharkov et al. 2011a; Zharkov et al. 2011b) and acoustic holography (Donea et al. 1999; Lindsey & Braun 1999; Donea et al. 2000; Lindsey & Braun 2000; Donea & Lindsey 2005; Zharkov et al. 2011a). The sunquake origin is normally indicated by a compact bright kernel (source) peaking during a flare, which is verified by statistical tests (Zharkov et al. 2011a). Some localised magnetic configurations are found to be more effective in channeling the energy and momentum to the lower atmosphere (Green et al. 2017).

The ripples were suggested to be the reflections from the solar surface of acoustic (in some cases, magneto-acoustic) waves induced by a sharp deposition into the solar interior of the momentum delivered by hydrodynamic shocks formed in flaring atmospheres (Kosovichev & Zharkova 1998; Zharkov 2013) produced, in turn, by hydrodynamic response to the injection of particle beams and travelling downward to the photospheric levels and solar interior with supersonic speeds (Somov et al. 1981; Fisher et al. 1985d,a; Allred et al. 2005; Zharkova & Zharkov 2007; Zharkova & Zharkov 2015). The other authors explored radiative back-warming as the other source of pressure transients producing acoustic waves in flares (Donea et al. 2006; Donea 2011). However, the observations showed that nearly half of sunquake locations are associated with little or absent white light emission (Matthews et al. 2011; Buitrago-Casas et al. 2015; Zharkov et al. 2011a). And the third mechanism of sunquakes generation can occur in the locations of Lorentz force transients, which, supposedly, produce a well-directed magnetic impulse of Poynting vector towards the photosphere and subsequent magneto-acoustic waves (Hudson et al. 2008; Fisher et al. 2012).

Recently, Macrae et al. (2018) detected a missing sunquake in the flare of 6 September 2011 in previously not acoustically active flare (Liu et al. 2014) and provided the first quantitative interpretation of the sunquake's properties (timing, directionality) using a hydrodynamic response to plasma heating by beam electrons as an input for the another hydrodynamic model for acoustic wave propagation in the solar interior. They demonstrated that, in fact, all three mechanisms associated with the generation of seismic signatures are present in flaring atmospheres when they have sunquakes. The energetic particles are likely to gain their energy from reconnecting current sheets of flares by converting with the help of Lorentz force the magnetic

energy into energetic particles. Then these relativistic electrons can over-ionise the ambient hydrogen plasmas by 5-6 orders of magnitude and keep this ionisation for up to 40 minutes by radiative transfer in optically-thick Lyman continuum (Druett & Zharkova 2019) leading to appearance of Balmer continuum emission and white light emission in Paschen continuum (Druett & Zharkova 2018).

Energetic particles accelerated in current sheets occurring on the top of flaring atmospheres (Zharkova et al. 2011) are found to deliver their energy to deeper layers of a flaring atmosphere causing its heating. During the impulsive phase of flares the injected particle beams are shown to precipitate into flaring atmospheres and heat them via Coulomb collisions (Brown 1971; Syrovatskii & Shmeleva 1972) causing hydrodynamic responses of flaring atmospheres (Somov et al. 1981; Fisher et al. 1985e; Allred et al. 2005; Zharkova & Zharkov 2007; Zharkova & Zharkov 2015). In the hydrodynamic models of type one the heating by particle beams of the quiet Sun (QS) chromosphere is shown to sweep the ambient plasma to lower atmosphere, forming a new flaring atmosphere with its own corona, transition region and chromosphere (Somov et al. 1981; Duijveman et al. 1983; Zharkova & Zharkov 2007). This sweeping of chromospheric plasma by precipitating beams is quickly followed by evaporation of this plasma back to the corona combined with strong hydrodynamic shocks propagating with supersonic speeds downward to the photosphere and beneath (Somov et al. 1981; Fisher et al. 1985a,e; Allred et al. 2005; Zharkova & Zharkov 2007; Zharkova & Zharkov 2015).

This hydrodynamic response of ambient plasmas heated by very intense beams lasting for only 5-10 seconds causes a formation of the new flaring atmosphere with a sharp increase of its temperature, decrease of the ambient density in the corona combined with hydrodynamic shocks in the chromosphere and strong macro-motion upwards and downwards associated with explosive evaporation of the chromospheric plasma into a flaring corona and propagations of hydrodynamic shocks towards the solar interior (Somov et al. 1981; Duijveman et al. 1983; Fisher et al. 1985e; Zharkova & Zharkov 2007; Zharkova & Zharkov 2015). There are other two models of hydrodynamic heating (in preheated atmospheres or isotropic heating) produce much milder chromospheric plasma evaporation without sweeping, combined with the shocks moving with much smaller velocities downwards to the lower atmosphere (Polito et al. 2016; Fisher et al. 1985b,e; Allred et al. 2005; Kennedy et al. 2015; Bradshaw & Cargill 2006). These models are not relevant for the atmospheres with large red-shifted line emission and sunquakes requiring a very strong moment deposition to lower atmosphere and solar interior to produce the ripples (Kosovichev & Zharkova 1998; Zharkova 2008; Donea 2011; Zharkova & Zharkov 2015).

In this paper we consider flaring atmospheres heated by short pulses of powerful particle beams remain heated for rather long time of 1-1.5 hours after the beam offset before they are fully cooled off to the pre-flare conditions (Somov et al. 1981; Duijveman et al. 1983; Fisher et al. 1985e; Zharkova & Zharkov 2007) travelling with the supersonic speeds to the flaring photosphere and solar interior for about 40-50 seconds (Macrae et al. 2018). These HD shocks are shown to induce

acoustic (and magneto-acoustic) waves in the solar interior seen as ripples on the solar surface, or sunquakes (Zharkov 2013). The shock speed profile for the 6 September 2011 flare was evaluated from the simulations and compared it with the sound speed in the solar interior that helped to define the key characteristics of acoustic waves formed in the solar interior by such the shock and to produce the first successful quantitative interpretation of the simultaneous seismic and optical signatures recorded for this flare of 6 September 2011 (Macrae et al. 2018).

In addition, it was shown (Zharkova & Kobylinskii 1993) that electron beams can cause essential non-thermal collisional ionisation and excitation of hydrogen atoms by beam electrons that strongly (by a few orders of magnitude) increases the excitation and ionisation degree of hydrogen atoms from all atomic levels. The non-thermal collisions and ionisation combined with plasma heating caused by beam electrons can lead to an increase in hydrogen line and continuum radiation in Lyman, Balmer and Paschen series that was recently verified with the detailed radiative hydrodynamic simulations using the HYDRO2GEN code (Druett et al. 2017; Druett & Zharkova 2018, 2019). The authors confirmed the enhancement of Lyman, Balmer and Paschen lines and continua of hydrogen atoms in flares caused by beam electrons. Druett & Zharkova (2019) showed that after the beam is switched off, the high ionisation degree of a flaring plasma gained during the beam injection is sustained for a very long time by Lyman continuum emission because of its large opacity. This leads to a long enhancement of Hydrogen ionisation in flaring atmospheres and an increase of Lyman  $\alpha$  and  $\beta$  line emission in the line cores and wings (Druett & Zharkova 2019).

Using the radiative hydrodynamic model HYDRO2GEN allowed to naturally explain the earlier wide-spectral filter observations with large (2-5 Å) red shifts (e.g. Ichimoto & Kurokawa 1984; Wuelser & Marti 1989) by propagation of hydrodynamic shocks formed in flaring atmospheres as the result of injection of electron beams (Druett et al. 2017; Druett & Zharkova 2018). Although, these large red shifts cannot be seen by modern instruments with narrow ( $\pm 1.5$  Å) spectral windows (Druett et al. 2017; Druett & Zharkova 2018) that explains the frequently reported delays of the order of 30 s of the appearance of H $\alpha$ -line emission with respect to HXR emission in powerful flares (Kaempfer & Magun 1983; Veronig et al. 2002; Radziszewski et al. 2011). Moreover, the simulations with HYDRO2GEN code also accounted for close timing and locations of HXR and WL emissions seen in the solar flares on the limb (Martínez-Oliveros et al. 2012) indicating the very close heights and timing of formation of these emissions in flaring atmospheres that was interpreted by the increased non-thermal ionisation of hydrogen atoms by beam electrons (Druett & Zharkova 2018) maintained by radiative transfer in Lyman continuum (Druett & Zharkova 2019).

In the current paper 2 we use the properties of flaring atmospheres heated by particle beams linked to detected H $\alpha$  kernels and sunquakes in the 6 September 2017 flare and simulate the hydrodynamic responses by these atmospheres to injection of particle beams whose physical parameters can be tested with the observed EUV, H $\alpha$ , white light and seismic signatures.

These simulations were extended to the investigation of production of seismic waves by using the hydrodynamic shocks generated in flaring atmospheres (HD models 1) as the initial condition for the hydrodynamic models 2 applied for generation of acoustic waves in the solar interior. This approach allows us to obtain the sets of acoustic waves in the interior and to detect their first bounces from the solar surface, or ripples, observed as sunquakes in the vicinity of these flaring atmospheres.

The hydrodynamic model 1 of flaring atmospheres heated by particle beams are discussed in section 2, the hydrodynamic shocks and their role in formation of Hydrogen H $\alpha$  emission with large red-shifts and white light emission are discussed in section 3, the hydrodynamic models of acoustic wave formation in the solar interior are explored in section 4 and general discussion of the results and conclusions are drawn in section 5.

## 2. Hydrodynamic heating of flaring atmospheres

The plasma of flaring atmosphere is heated by injection of particle beams injected into the chromosphere of the quiet Sun (QS) from the primary energy release point in the corona and precipitating from the top boundary with the heating function derived from flux conservation equation (Brown 1971), continuity equation (Syrovatskii & Shmeleva 1972) or Fokker-Planck equation (Gordovskyy et al. 2005; Siversky & Zharkova 2009). The beam electrons are assumed to heat the cold ambient chromospheric plasma, sweeping it as a piston to deeper atmospheric levels (Syrovatskii & Shmeleva 1972). This heating prompts a hydrodynamic response of the ambient plasma turning the QS chromosphere into a flaring atmosphere (Somov et al. 1981; Zharkova & Zharkov 2007).

### 2.1. Brief summary of the detected flaring events

The X9.3 flare on September 6, 2017 started at 11:55:37 UT at the solar disk location S09W34 and comprised two flaring events : flaring event 1 (FE1) starting at 11:55:37 UT and flaring event 2 (FE2) starting at 12:06:40 UT described in Paper 1 (Zharkov et al. 2020). The non-linear force-free field (NLFFF) restoration of magnetic field in the active region 12673 prior to the X2.2 flare followed by 3D MHD simulations of magnetic field dynamics during the two solar flaring events of X-class occurred on the 6 September 2017 (Inoue et al. 2018) revealed that after the X2.2 flare and prior to the X9.3 flare there were three magnetic flux ropes (MFRs) formed with very braided and twisted magnetic structures shown in Fig. 1a. The places, where the three magnetic flux ropes are embedded into the photosphere, or the rope footpoints named as F1-F6 are close to the locations of the 4 sunquakes shown in Fig. 1b as detected in Paper 1.

We intend to explore physical conditions in the flux ropes, which produced four (possibly five) seismic sources, the locations of which are indicated by the asterisks in the HMI white light image in Fig. 1b. The asterisks indicate the locations from which the time-distance diagrams of sunquakes (seismic sources 1-3) or holography sources (1-4) are obtained. The H $\alpha$

kernels 1 and 2 are detected in the locations of the seismic sources 1 and 2 in the flaring event 1 and H $\alpha$  kernel 3 detected in the same location as the seismic source 2 but during the flaring event 2 where, we suggest, the potential seismic source 5 is likely to occur.

### 2.2. Heating by particle beams

This flare had at least four flaring events detected in Lyman- $\alpha$  line emission, which were observed without spatial resolution by GOES, and LYRA instruments with soft X-ray (SXR) and Lyman- $\alpha$  light curves indicating the times for each event (Hochedez et al. 2006; Dominique et al. 2013). From these flaring events we investigated two events FE1 and FE2. For FE1 we have high energy HXR and gamma-ray (GR) observations by KONUS/WIND payload without any spatial resolution (FE1)(Lysenko et al. 2019). There were no HXR observations for FE2. The only HXR observations by the RHESSI payload (spatial resolution 2'') were obtained more than one minute later after the FE2 onset. Hence, we have to use the areas on H $\alpha$  kernels to account for the areas of footpoints where particle beams precipitate and produce HXR emission reported by KONUS payload and to link these kernels by times of occurrences and locations to detected sunquake 1 (SQ1), sunquake 2 (SQ2) and sunquake 3 (SQ3) for FE1 and hypothetical SQ5 and H $\alpha$  kernel for FE2.

Thus, in order to derive the specific conditions in the atmospheres leading to the observed seismic sources 1-3 associated with FE1 we involved H $\alpha$  kernels observed with high spatial resolution (0.06'') by CRISP/SST instrument giving us the areas of the footpoints and characteristics of the seismic sources themselves. Based on the observations during the flaring event 1 when three seismic sources were detected of strong HXR and GR emission (both continuous and nuclear lines) by the KONUS payload without any spatial resolution (Lysenko et al. 2019) indicating to presence of electrons and protons/ions heating the flaring atmospheres, we need to consider mixed beams injected into these footpoints with the equal proportion of electrons (50%) and protons (50%), in the absence of any tools to assume otherwise, which can produce the overall HXR and GR emission observed at this event.

We use the averaged in time HXR energy spectrum derived from the KONUS instrument, from which we derive the averaged spectral index of 4, and total power of the beam about  $1.1 \cdot 10^{31}$  erg (see discussion in Lysenko et al. 2019). Moreover, in the discussion of their paper, p.11 Lysenko et al. (2019) report that during the initial impulsive phase the lower energy part of the HXR spectrum revealed the soft-hard-soft (SHS) pattern indicating that the beam, which heats the flaring atmospheres in this event. We conclude that this beam had to have a large initial energy flux increasing and decreasing in time as a triangle function, following the kinetic Fokker-Planck solutions (Zharkova & Gordovskyy 2006) pointing that the SHS pattern in HXR energy spectrum indicates a presence of strong return currents, if the beam energy flux becomes much higher than  $1 \cdot 10^{11}$  erg  $\cdot$  cm $^{-2}$  s $^{-1}$ .

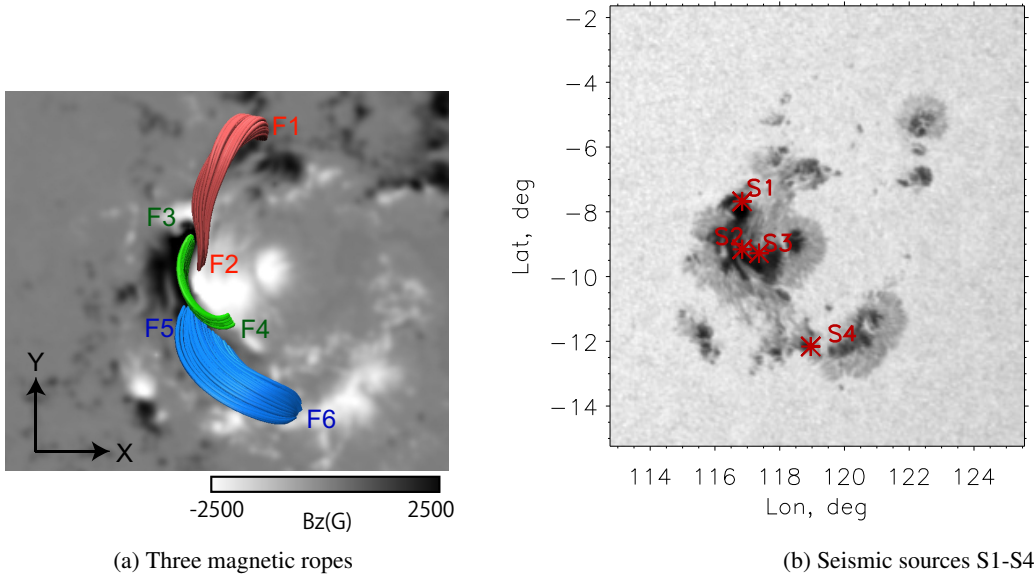


**Fig. 1.** The magnetic flux ropes formed prior to the 9.3X flare of 6 September 2017 derived from NLFFF magnetic field reconstruction and MHD simulations by Inoue et al. (2018) (a) and the locations of four sunquakes detected for the flare (b) adopted from Paper 1.

For the flaring event 1, induced by the mixed beam with total energy of  $1.2 \cdot 10^{31}$  erg by using the observed areas of  $H\alpha$  line kernels 1 and 2 and assuming that the area of footpoint for the  $H\alpha$  kernel 3 was similar to that in the kernels 2, and by looking at the shapes of  $H\alpha$  line profiles, or their blue wings, seen in all three kernels, we derived in Paper 1 (Zharkov et al. 2020) the initial energy flux of the beam to vary between  $(8 - 12) \cdot 10^{12} \text{ erg} \cdot \text{cm}^{-2} \text{ s}^{-1}$  depending on the area of a particular kernel or seismic source. In the absence of other options, we still can use a spectral index of 4 for these beams derived from the KONUS observations.

From the fact of a very strong sunquake 2 present in the kernel 2 in the footpoint F4 (southern footpoint of the green rope) and our previous simulations of  $H\alpha$  line profiles (Druett et al. 2017; Druett & Zharkova 2018) it looks very likely that a strong mixed beam was injected into this footpoint, where protons can deliver the sufficient momentum to lower atmospheric levels and can also account for the increase of  $H\alpha$  line emission in this location. The  $H\alpha$  line profile observed in the kernel 2 has a lower blue wing intensity than in kernel 1, while its area is close to that of kernel 1 indicating that the blue wing in kernel 2 is located further from the line core than in kernel 1, e.g. the red shift in kernel 2 is larger than in kernel 1 meaning that the mixed beam in kernel 2 should have a higher initial flux than in the kernel 1. Hence, we suggest that the initial energy flux of the beam in kernel 1 can range in  $(7 - 9) \cdot 10^{12} \text{ erg} \cdot \text{cm}^{-2} \text{ s}^{-1}$ .

For the flaring event 2 from a comparison of the blue wing intensities and shapes observed from  $H\alpha$  kernels 2 and 3, it is possible to suggest that the beam with similar parameters as in kernel 2 could be injected into the atmosphere produced at 12:06:40 UT the kernel 3 in the footpoint F5 of the blue rope that was 10 minutes later the kernel 2 in seismic source 2. RHESSI started its observation at 12:08 UT, so we can only

use the electron parameters derived from RHESSI for a general guidance assuming sympathetic flares occurring in succession in the same magnetic configurations but not for a direct indication of the energetic particle parameters.

Based on the observations of strong hard X-ray emission in FE1 and assuming the similar input in FE2, based on the similarity of  $H\alpha$  line blue wings in kernels 2 and 3 we assume that flare emission in the both flaring events was produced by the injection of sub-relativistic mixed beams with power-law energy distributions and initial energy fluxes of  $(8 - 12) \cdot 10^{12} \text{ erg} \cdot \text{cm}^{-2} \text{ s}^{-1}$  and spectral index of 4. These beams are assumed to produce heating of flaring atmospheres in Coulomb collisions (Brown 1971; Syrovatskii & Shmeleva 1972). The beam parameters can be further tuned by the fit to the  $H\alpha$  line profile observed in kernels 1- 3 discussed in section 3.

### 2.3. Hydrodynamic response of flaring atmospheres

For the physical conditions of flaring atmospheres we use the models of hydrodynamic responses of the ambient plasma to short pulses of energy deposition by very intense energetic electron or mixed beams precipitating from the corona to the lower atmosphere (hydrodynamic model of type 1 discussed in the Introduction) (Somov et al. 1981; Zharkova & Zharkov 2007). The hydrodynamic model considers two energy equations (for electron and ion components), momentum and continuity equations to describe the ambient plasma response to heating by beam electrons (Somov et al. 1981; Zharkova & Zharkov 2007) using a Lagrangian coordinate  $\xi$ . Plasma heating is caused by particle beams (Syrovatskii & Shmeleva 1972; Gordovskyy et al. 2005) and plasma cooling is caused by the viscosity, or motion between electrons and ions (Somov et al. 1981; Zharkova & Zharkov 2007). We consider the radiative

energy losses in the corona (Cox & Tucker 1969) and by hydrogen emission in the chromosphere (Zharkova & Kobylinskii 1993; Kobylinskii & Zharkova 1996).

These models have the initial conditions of a quiet Sun chromosphere starting from a column depth just below the quiet Sun's transition region ( $\xi = 10^{17} \text{ cm}^{-2}$ ) down to the beginning of the upper photosphere ( $\xi = 10^{22} \text{ cm}^{-2}$ ). Details of these initial conditions are given in Somov et al. (1981), and include (a) a constant temperature of 6,700K derived from semi-empirical calculations shown by straight line in Fig. 2a, (b) hydrostatic equilibrium  $v(0, \xi) = 0$ , (c) a density distribution as defined by the straight line in the logarithmic plot of Fig. 2b. The numeric method for calculation of the hydrodynamic response in a flaring atmosphere to injection of power-law beam electrons is described in detail in the previous papers (Somov et al. 1981; Zharkova & Zharkov 2007).

The duration of beam injection is chosen as 10 s, the initial energy flux of a beam varies as a triangular function in time, with maximum between five and six seconds (Zharkova & Zharkov 2007). After solving the system of four partial differential equations with the initial and boundary conditions for precipitating electron beam with given parameters (initial energy flux  $F_0$  and spectral index  $\gamma$ ) we obtain time-dependent distributions of electron  $T_e$  and ion  $T_i$  temperatures, ambient plasma density  $T$  and macrovelocities,  $v$ .

Heating of the QS chromosphere by a short pulse of a very intense beam of electrons or protons, or mix of them (model of type 1) (Somov et al. 1981; Duijveman et al. 1983; Zharkova & Zharkov 2007; Druett & Zharkova 2018) is shown to sweep the ambient plasma to the lower atmosphere, forming a new flaring atmosphere with a new corona, transition region and chromosphere. This sweeping is followed by the plasma evaporation back to the corona combined with formation of a low-temperature condensation in the chromosphere moving as a shock to the photosphere. A hydrodynamic heating in the other two types of models (preheated and isotropic) would result in mild chromospheric plasma evaporation without sweeping, combined with the less intense shock moving downwards to the lower atmosphere with much smaller velocities and to much smaller depth on the surface instead reaching the solar interior (Polito et al. 2016; Fisher et al. 1985b,e; Allred et al. 2005; Kennedy et al. 2015; Bradshaw & Cargill 2006), which are not relevant for the atmospheres associated with sunquakes.

## 2.4. Simulation of hydrodynamic responses

Hydrodynamic responses of flaring atmosphere caused by 10 second pulses heating by intense particle beams (either mixed or pure electrons) are shown to lead to quick sweeping of the quiet sun (QS) chromosphere plasma towards the photosphere and beneath forming hydrodynamic shocks which are shown to first move with large velocities towards the solar interior and to later return to the pre-flare conditions. The phases of this process include the initial heating by beam particles in Coulomb collisions lasting ten seconds after the beam onset, which produces a hydrodynamic response of the ambient plasma to this heating followed by slow cooling off of the am-

bient plasma and its return to the pre-flaring position and conditions. Hydrodynamic responses start to develop over a minute after the beam onset and last up to an hour because of a larger characteristic hydrodynamic time (order of 30 seconds) caused by thermal diffusion (Shmeleva & Syrovatskii 1973).

Hence, the hydrodynamic simulations for the flaring atmospheres heated by a mixed beam in the footpoints associated with the seismic sources 2 and 3 are plotted in Fig. 2 (left column). We also run the other hydrodynamic simulations with the lower initial energy fluxes reduced by an orders of the magnitude down to the initial energy fluxes of  $10^{11} \text{ erg} \cdot \text{cm}^{-2} \text{ s}^{-1}$  and  $10^{10} \text{ erg} \cdot \text{cm}^{-2} \text{ s}^{-1}$  (see the plots in Druett & Zharkova 2018, not shown here) used in a comparison of simulated and observed  $\text{H}\alpha$  line emission. For a comparison of the current conditions for sunquake 2 with the conditions of the sunquake formation in the flare of 6 September 2011, in Fig. 2 (right column) we present the hydrodynamic models simulated for the injection of an electron beam with the initial energy flux of  $4.3 \cdot 10^{11} \text{ erg} \cdot \text{cm}^{-2} \text{ s}^{-1}$  and spectral index of 4 (Macrae et al. 2018). These two hydrodynamic models can provide important insight into the mechanisms of formation of the acoustic signatures in two flares discussed in section 4.2.2.

It can be noted that the hydrodynamic responses induced by a mixed beam (Fig. 2, left column) in flare of 2017 and by electron beam (Fig. 2, right column) in flare 2011 are very different despite they both show a quick increase of the kinetic temperatures within the first 5 seconds after the beam onset. However, compared to the initial chromospheric temperature of 6700K, the mixed beam causes a much stronger increase of the kinetic electron temperature in the corona up to 40 million Kelvin (MK) (Fig. 2a), while the kinetic temperature increase by less intense beam is found increasing only to 10 MK. The ambient plasma density in the atmosphere heated by either beams (Fig. 2b) is significantly reduced in the flaring corona, from the initial QS chromospheric magnitude ( $10^{10} \text{ cm}^{-3}$ ) to  $10^9 - 10^8 \text{ cm}^{-3}$ , to form the new corona of a flaring atmosphere (Somov et al. 1981). As expected, during the time of the beam injection (10s) there is also a larger reduction of the coronal density swept by precipitating mixed beam compared to the electron one (see Fig. 2b). These trends are similar to the hydrodynamic models heated by electron beams with the same parameters reported by Fisher et al. (1985a,d).

This stronger plasma sweeping in the flaring atmosphere by the mixed beam leads to a larger speed of chromospheric plasma evaporation back to the corona that approaches 1600 km/s compared to 1300 km/s for an electron beam as shown in Fig. 2c (compare the left and right plots). Furthermore, the fast dynamics of the coronal plasma heating by a mixed beam leads to very strong, explosive, evaporation (with velocities above 1500 km/s) of the chromospheric plasma to the coronal levels up to 8000 km above the surface, while the electron beam would cause much milder evaporation to the heights of about 1500 km above the surface approaching the macrovelocities just above 1200 km/s.

The upward motion of the flaring plasma is reflected in the macrovelocity plots (Fig. 2c), showing negative (upward) macrovelocities corresponding to the evaporation of chromospheric plasma upwards to the newly formed corona at the

column depths between  $10^{17}$  and  $10^{19} \text{ cm}^{-2}$ . This evaporation lasts for a one-two thousand seconds even after the beam is stopped expanding with the increasing velocities upwards to the QS corona (Somov et al. 1981; Fisher et al. 1985c,e; Zharkova & Zharkov 2007). The evaporation velocities range from a few tens of  $\text{km}\cdot\text{s}^{-1}$  (at 1s) up to  $1500 \text{ km}\cdot\text{s}^{-1}$  (at 30–100 s). As shown earlier (see section IV and Fig. 5 in Fisher et al. 1985c), these high upflow velocities naturally appear in the gasbag models (Somov et al. 1981; Fisher et al. 1985c; Zharkova & Zharkov 2007). These higher velocities of evaporation, are larger than those measured in the EUV observations by the older missions (Doschek et al. 1979; Antonucci et al. 1982; Zarro et al. 1988) as well by the modern instruments like the EIS/Hinode, the Atmospheric Imaging Assembly (AIA/SDO) (Lemen et al. 2011) or the EUV variability Experiment (EVE/SDO) (Woods et al. 2006; Doschek et al. 2014; Milligan et al. 2014; Milligan 2015).

However, the lack of the observations with high upflow velocities above  $1000 \text{ km/s}$  can occur on a few reasons: a) the dynamic range of the CCD sensors whose extra-exposure time during a flare onset, if not reduced, can lead to the over-exposed emission in hot coronal lines, where such large upflow velocities are expected to occur; b) the coronal density at the upper heights where these velocities occur becomes too low as shown by hydrodynamic simulations (Fig.2b), so the abundances of hot ions with large upward motion on the line of sight are not sufficient to produce a notable emission, e.g. the emission measures are too weak; c) the lines selected by the EUV instruments can only observe lower temperature plasma formed at the lower corona where the macrovelocities are restricted up to  $400 \text{ km}\cdot\text{s}^{-1}$  (Doschek et al. 2014; Milligan 2015).

While the theoretical hydrodynamic temperature and macrovelocity curves show strong increase of the temperature up to  $40 \text{ MK}$  and macrovelocities exceeding  $1400 \text{ km/s}$ , which cannot be observed by the modern instruments with restricted dynamic ranges of physical parameters of the hot plasma of solar corona and transition region or lower densities of the flaring corona plasma after sweeping by very powerful particle beams. Evidently, after the beams are switched off, the plasma cooling in the upper atmosphere heated by mixed beams (left column) is much slower than in the atmosphere heated by the electron beam (Fig. 2, compare left and right columns). Thus it would be beneficial to observe the emission in these hot coronal levels in very hot lines allowing to catch large plasma upflows with the future instruments for SXR observations of hot coronal plasma with wider energy ranges.

Besides large upflows, the abrupt energy deposition by super-energetic particle beams within a short timescale of 10 seconds leads to a formation in the flaring chromosphere of low temperature condensations, which move downwards to the photosphere and interior with supersonic velocities as shocks, thus producing large downflows (Somov et al. 1981; Zharkova & Zharkov 2007; Zharkova & Zharkov 2015). From comparing the panels in Fig.3 for different times after the beam injection it is evident that the higher the initial energy flux the larger the speed of a shock produced by hydrodynamic response. For example, for the mixed beam the shock velocities of  $50 - 100 \text{ km}\cdot\text{s}^{-1}$  are reached just 1 second after the beam

onset (see Figs. 2c and 3a) while after 5 seconds these velocities sharply increase to  $200 - 250 \text{ km}\cdot\text{s}^{-1}$  for weaker beam (see Figs. 2c, right plot and 3a) and  $380-400 \text{ km/s}$  for more intense beam (see Figs. 2c, left plot and 3b). The plasma of the shocks has a slightly (up to  $10^4 \text{ K}$ ) increased temperatures and much larger densities (a factor of  $10^{13} \text{ cm}^{-3}$  up to  $10^{14} \text{ cm}^{-3}$ ) for the most powerful mixed beam (Fig. 2b, left plot).

Hence, these shocks have large densities and high macrovelocities being capable of delivering very large momenta to the lower atmosphere and solar interior. It is important to determine how deeply these shocks can travel into the QS solar atmosphere. For a comparison, in order to clarify this point, we present in Fig. 4 the relationship between the linear depth of the quiet Sun (axis Y) versus the column depth of a flaring atmosphere (axis X) for the beams with the initial fluxes of  $10^{12} \text{ erg/cm}^2/\text{s}$  (a) and  $10^{11} \text{ erg/cm}^2/\text{s}$  (b). It is evident that the weaker beam in Fig.4b sweeps the ambient plasma downward to a column depth of 1-2 units of  $10^{19} \text{ cm}^{-2}$ , or particle density about  $10^{13} \text{ cm}^{-2}$  that is just close to the quiet Sun surface if compared with the linear depth shown in Fig.4. While the stronger beam shown in Fig.4a has much greater power and thus, it sweeps the ambient flaring plasma down to the column depth of  $10^{20} \text{ cm}^{-2}$  with a density of factor of  $10^{13} \text{ cm}^{-2}$  that is below the QS solar surface, appearing in the solar interior. Hence, both shocks move with a supersonic speed into the deep solar interior.

Therefore, the shock produced by a more intense beam (Fig.4a) starts its motion deeper in the interior than the shock driven by the weaker beam (Fig. 4b), and it has a larger density, thus, delivering a larger momentum while moving from the deeper interior depth. This means that the weaker beam forms a shock just beneath the photosphere and this shock travels with a supersonic speed in the solar interior a distance of  $<1000 \text{ km}$ , when it travels with the speed higher than the local sound speed (Zharkova & Zharkov 2007; Macrae et al. 2018). In contrast, the more intense beam, which sweeps the ambient plasma much deeper into the solar interior, forms the shock inside the solar interior at larger depth from the solar surface, and travels for the larger distance  $>1000-1500 \text{ km}$  in the solar interior with a supersonic speed (Zharkova & Zharkov 2015). These differences in the depth of deposition, velocity and density of the shocks will affect the conditions for formation of acoustic waves in the solar interior. The investigation of the shocks derived for physical conditions in the 6 September 2011 and 2017 flares is presented in section 4.

## 2.5. Probing hydrodynamic results with the EIS observations

The HD models heated by the mixed beam produce within 5-15 seconds very fast heating of a flaring atmosphere above  $40 \text{ MK}$  that may explain an early brightening of flaring atmosphere in  $1700 \text{ Å}$  leading to its over-exposure of this AIA emission. For the HD model caused by the powerful mixed beam the EUV emission can be observed by EIS instrument in He II and Fe XXIII emission at the very beginning of the flare onset if the flaring atmosphere temperature approaches the temperature

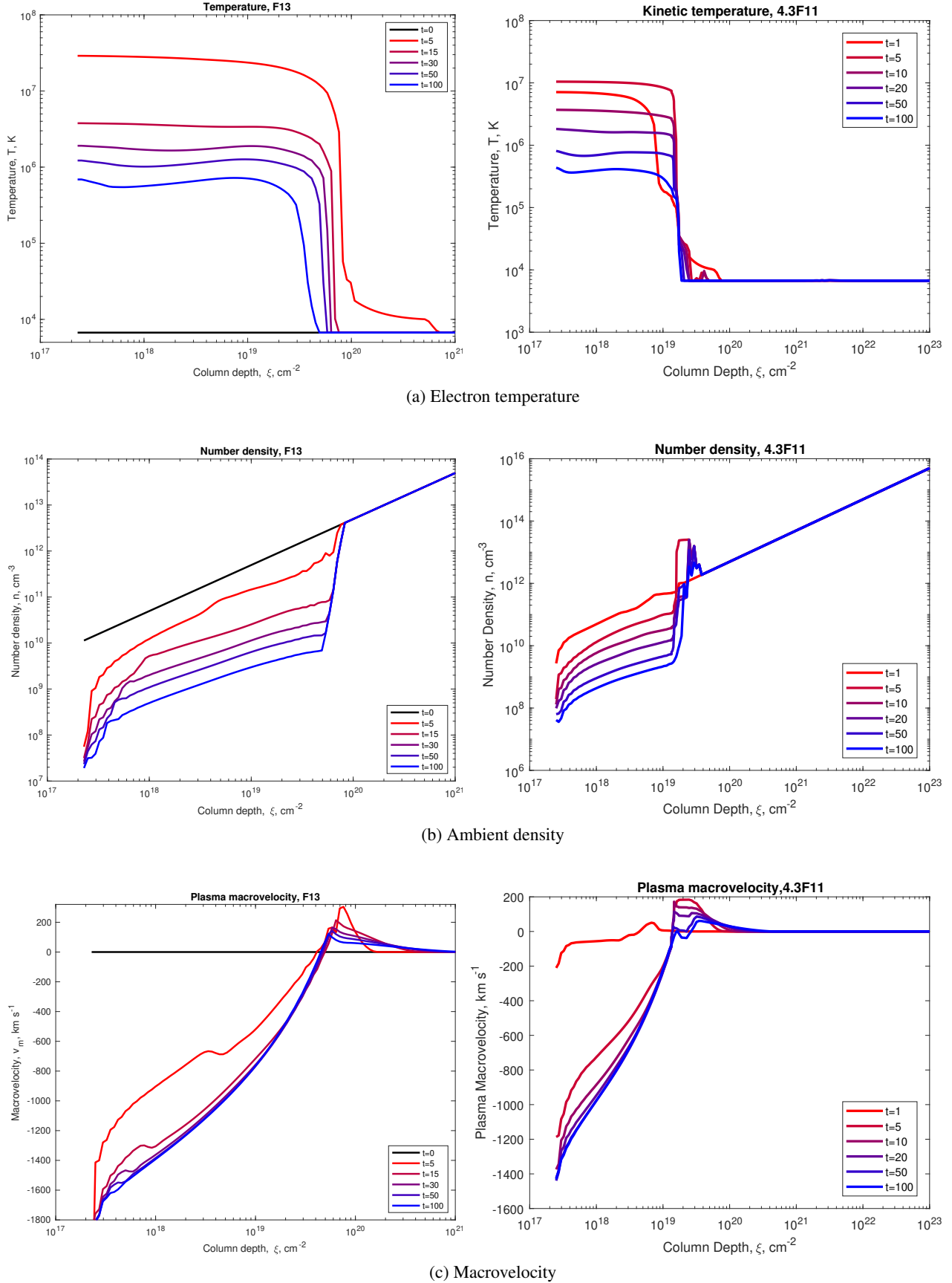


**Fig. 2.** The simulated hydrodynamic responses of flaring atmospheres to the injection of power-law particle beams with the initial energy flux of  $f 1.0 \times 10^{13} \text{ erg}\cdot\text{cm}^{-2}\cdot\text{s}^{-1}$  and spectral index 4 (left column) and with the initial energy flux of  $4.3 \times 10^{11} \text{ erg}\cdot\text{cm}^{-2}\cdot\text{s}^{-1}$  and spectral index 3.5 (right column) showing the column depth dependencies of electron kinetic temperature, K (top row), ambient plasma densities,  $\text{cm}^{-3}$  (middle row) and plasma macrovelocities,  $\text{km}\cdot\text{s}^{-1}$  (bottom row).



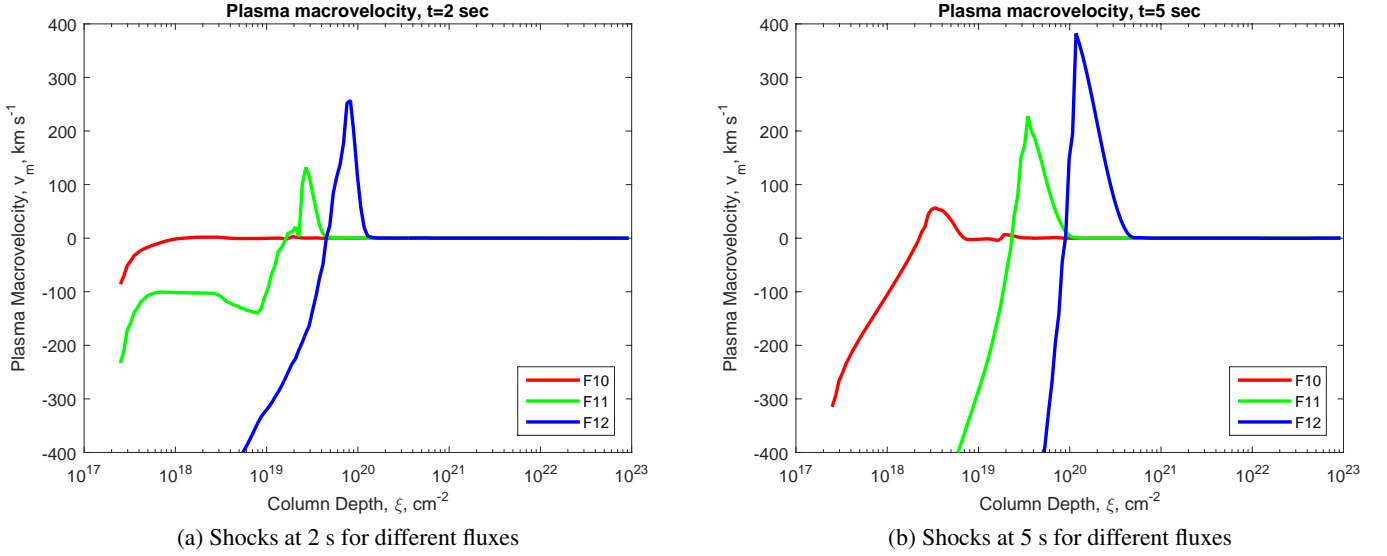


**Fig. 3.** Left panel: a close look-up at the macrovelocities of the shocks produced by electron beams in the first 2 s (a) and 5 s (b) after the beam onset for different initial energy fluxes and the same spectral index of 3.

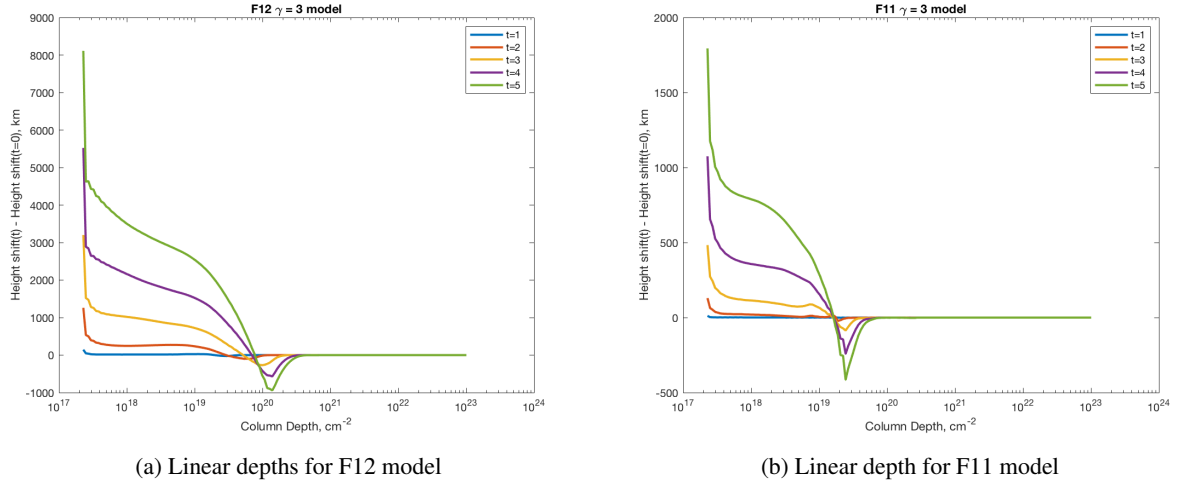


**Fig. 4.** The linear depths (Y-axis) versus column depths (X-axis) of hydrodynamic responses of a flaring atmosphere to the injection of a beam with the initial flux of  $f 1.0 \times 10^{13} \text{ erg cm}^{-2} \text{ s}^{-1}$  (left)  $1.0 \times 10^{11} \text{ erg cm}^{-2} \text{ s}^{-1}$  (right) and spectral index of 3.0. Note, the zero point in axis Y indicates the position of the quiet Sun photosphere.

range suitable to the radiation temperatures of these transitions: 7-20 million K for Fe XXIII and about  $10^5$  K for He II line. It can be seen that the temperature magnitudes favourable for this Fe XXIII emission appear immediately during the beam onset and continue to exist after the beam offset while at 15-30 seconds from the event start the atmosphere is cooling to a few million K shown by the dark red and purple lines in Fig. 2a. The emission of He II line is expected to appear in this model a bit (30-50 seconds) later after the beam offset. By the time of 50 seconds, the hydrodynamic shock velocity is also reduced if heated by a mixed beam (see Fig. 2c, left plot) or even this shock becomes returning to the pre-flare atmospheric level if heated by an electron beam (compare the left and right plots of Fig. 2c).

The explosive evaporation of the plasma heated by a mixed beam starts from the very first seconds of observations with high macrovelocities of  $100 \text{ km s}^{-1}$  (see paper 1 Zharkov et al. 2020), similar to the macrovelocities simulated in the lower flaring corona (Fig. 2c, left column) for a mixed beam, and approaching the velocities of  $400\text{-}500 \text{ km s}^{-1}$  only 5 seconds after the beam onset. Later these macrovelocities are reduced to  $250 \text{ km/s}$  at 30-50 s after the event onset when these magnitudes are observed by Fe XXIII line (shown in Figs. 10-12 in Paper 1). As shown in paper 1, the spectrograms for the Fe XXIII 263.76 Å line for the event 1 occurring in FP3 of seismic source 1 reveals the large blue-shifted velocities of the upflows of  $400 \text{ km s}^{-1}$ , similar to the simulated velocities for heating by a mixed beam (blue line in Fig. 2c, left plot). Moreover, for



SQ2 the blue shifts in the line of Fe XXIII 263.76 Å show the macro-velocity of explosive evaporation exceeding 400 km/s much faster than in the atmosphere with SQ1 that indicates a stronger shock occurring in the location of SQ2, which, in turn, led to the observation of secondary ripples, or the additional ridge in time-distance diagram, constituting a double bounce of acoustic waves in the interior beneath the flare.

This is combined with the downflows of  $> 100\text{--}200\text{ km s}^{-1}$  seen in the He II spectrograms associated with SQ 1 and SQ2. The EIS observations in He II 256 Å in the locations of SQ1 and SQ 2 appear 30 s after the onset of FE1 confirming the starting time of the SQ1 and SQ2 20–25 s earlier than the red shift in He II line, which exists for about a minute shown in the first three bottom plots in Figs. 9 and the most three right plots in Fig. 10 in paper 1. It can be noted that this He II line captures first the downflows, which are followed in a minute or so by upflows with the magnitudes of macro velocities close to those predicted by the hydrodynamic (HD) simulations for the heating by a mixed beam (in SQ 1 and SQ 2) shown in Fig. 2 (left column). It can be seen that blue line shows the upwards macrovelocities in Fig. 2c approaching 400 km/s, similar to that measured in Paper 1 by the EIS instrument for the location of seismic source 1. At the same time, the downward motion modelled for this event also reaches the macrovelocity of 150–200 km/s (purple line in Fig. 2).

However, the He II 256 Å spectrograms with Doppler velocity taken in the location of a largest sunquake described in Paper 1 reveal the red-shifts approaching several hundred  $\text{km s}^{-1}$ , similarly to the simulations shown in Fig. 2c, left plot, to appear 15–20 seconds after the plasma started cooling off to the temperature when He II emission becomes observable. The simulated and measured blue shifts start from 150 km/s approaching 300 km/s within a short timescale of 15–30 seconds. The observed red-shifts in excess of  $250\text{ km s}^{-1}$  are well-correlated with the largest sunquake 2 in the footpoint FP4 associated with the green magnetic rope (see Fig. 1).

Also in the flaring event 2 the EIS in He II 254 Å observed both blue shifts up to two hundred  $\text{km s}^{-1}$  reported in paper 1, while the red-shifts in excess of  $150\text{ km s}^{-1}$  are well-correlated with the possible sunquake 5 and H $\alpha$  kernel 3, which seem to have the similar heating and seismic response as it was in seismic source 2. These observations still can be explained by the hydrodynamic simulations of the atmosphere heated by the powerful mixed beam shown in Fig. 2 (left column).

### 3. Radiative response of hydrogen atoms

#### 3.1. Description of radiative model

Based on the hydrodynamic models calculated above and in other our papers (Druett et al. 2017; Druett & Zharkova 2018, 2019) and taking into account that the characteristic hydrodynamic time (30 s) (Shmeleva & Syrovatskii 1973; Somov et al. 1981) is much longer than the characteristic radiative time (a fraction of a second) (Shmeleva & Syrovatskii 1973), one can apply the radiative models for hydrogen emission to the hydrodynamic models calculated for each second. The hydrogen emission in a flaring atmosphere was calculated using the sec-

ond part of HYDRO2GEN code utilising a full non-LTE approach for a five level plus continuum hydrogen model atom considering radiative transfer in Lyman series, Lyman continuum as well as in Balmer and Paschen ones (Druett et al. 2017; Druett & Zharkova 2018, 2019).

We consider the hydrogen atom excitation and ionisation by thermal and beam electrons as well by external and diffusive radiation (radiative transfer). The radiative transfer and statistical equilibrium equations were solved numerically by iterations defining the source functions in each atomic transition and ionisation degree of hydrogen atoms (Druett & Zharkova 2018) in the atmosphere at any given instant of the hydrodynamic response. The solutions of the radiative transfer equations were found using the L2 approximation introduced by Ivanov & Serbin (1984). The simulated H $\alpha$  line intensities are calculated from the source functions derived for atomic transitions between levels 3 and 2 using Voigt's absorption profiles (Druett & Zharkova 2018).

For non-thermal hydrogen excitation and ionisation rates by beam electrons the analytical formulae were used derived by Zharkova & Kobylinskii (1993), where it was shown that non-thermal collisional excitation and ionisation rates of hydrogen dominate above the thermal ones in flaring atmospheres from the chromospheric depths just below the transition regions (see Fig. 3 in Zharkova & Kobylinskii 1993). The stimulated photo-excitation by external radiation, de-excitation, and ionisation rates by thermal electrons for given physical conditions in flaring atmospheres were also taken from Zharkova & Kobylinskii (1993).

#### 3.2. Simulated H $\alpha$ line profiles and their fits to observations

In the X9.3-class flare on 6 September 2017 for the flaring event 1 we managed to detect a noticeable increase of H $\alpha$  line emission in the two H $\alpha$  kernels 1 and 2, and for the flaring event 2 in the H $\alpha$  kernel 3. Although the extracted emission line profiles in these kernels 1–3 were rather unusual with the emission increasing with the wavelengths over 3 Å (spectral window of the CRISP instrument) as reported in Paper 1 (Zharkov et al. 2020). The H $\alpha$ -line profile derived in kernel 1 coinciding with the seismic source 1, is located in footpoint F3 at the northern end of the green magnetic rope (see Fig. 1a). The H $\alpha$ -line kernel 2 was co-temporal with seismic source 2 and is located in the footpoint F4 at the southern end of the green magnetic rope in Fig. 1a. There was no any H $\alpha$ -line kernels detected in the location of seismic source 3, which has the most peculiar dynamics to be described in a forthcoming paper. The H $\alpha$  line emission in kernel 3 is occurred in the location close of that of seismic source 2 but during the flaring event 2 about 10 min later than in kernels 1 and 2. We assumed than in the kernel 3 there should be also a seismic source 5 occurred in the location close to F4 during the FE2.

In general, the hydrodynamic radiative simulations of hydrogen emission show that during the flare at the very first seconds after the beam onset, H $\alpha$  becomes an emission line revealing a strong increase of the central and wing emission

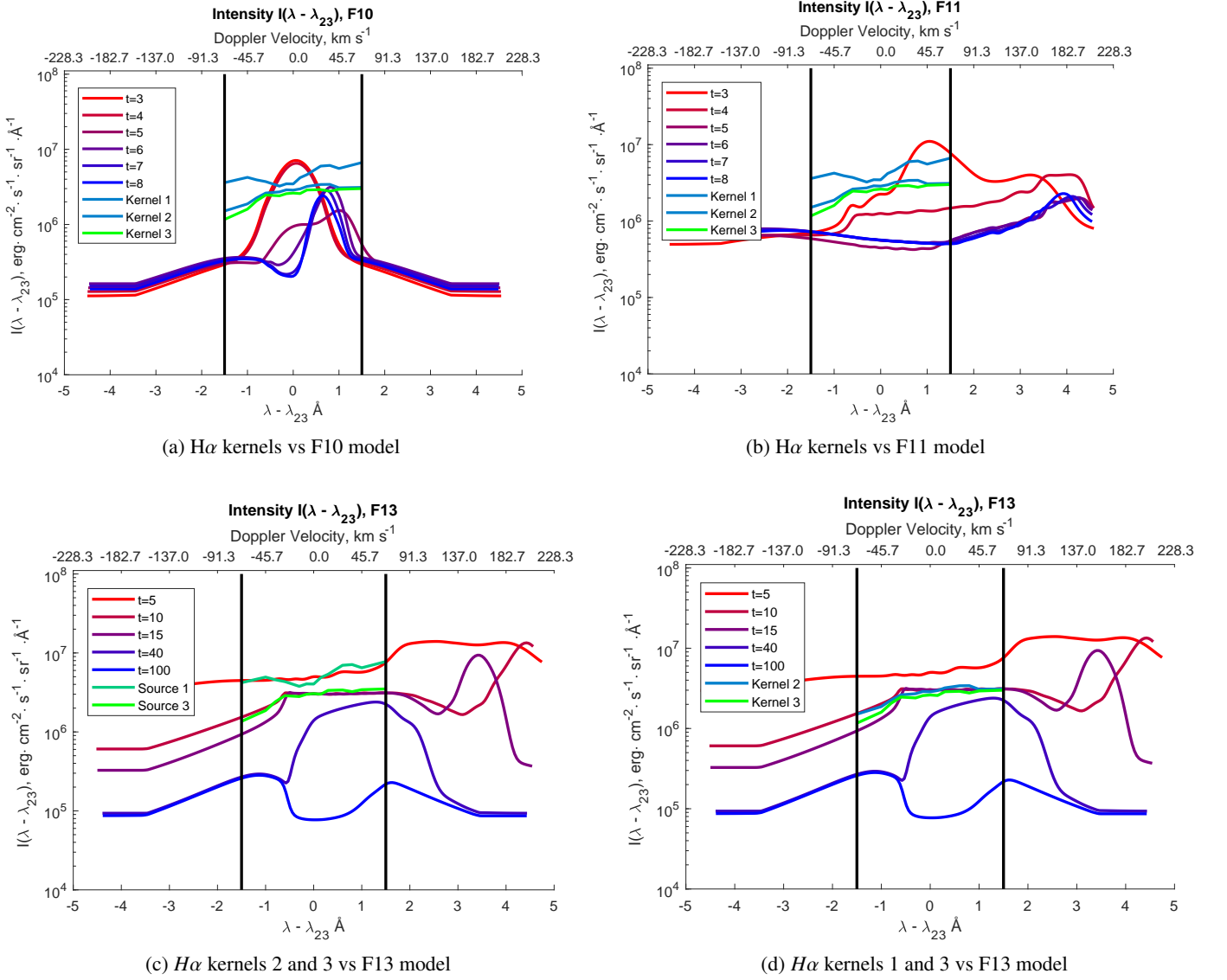


**Fig. 5.** The observed  $H\alpha$ -line profiles in kernels 1-3 overplotted on the  $H\alpha$  line profiles simulated with HYDRO2GEN code (Druett & Zharkova 2018) in flaring atmospheres produced by: (a) an electron beam with spectral index 4 and the initial energy flux of  $10^{10} \text{ erg} \cdot \text{cm}^{-2} \text{s}^{-1}$ ; (b) an electron beam with spectral index 4 and the initial energy flux of  $10^{11} \text{ erg} \cdot \text{cm}^{-2} \text{s}^{-1}$ ; (c) a mixed beam with spectral index of 4 and initial energy flux of  $10^{13} \text{ erg} \cdot \text{cm}^{-2} \text{s}^{-1}$ ; (d) a mixed beam with the same parameters as in c). The observed  $H\alpha$  line profiles are shown in kernel 1 (blue line), kernel 2 (light blue line) and kernel 3 (green line). The vertical lines show the spectral window  $\pm 1.5 \text{ \AA}$  for the CRISP/SST  $H\alpha$  line observations.

caused by enhanced ionisation and excitation induced by energetic power-law electron beams (Druett et al. 2017; Druett & Zharkova 2018). Furthermore, in the very first seconds,  $H\alpha$  line profiles become strongly redshifted as shown in Fig. 5 calculated for different particle beam parameters, similar to what has been observed in the past in the other flaring events with spectral windows of  $\pm 8 \text{ \AA}$  (Ichimoto & Kurokawa 1984; Wuelser & Marti 1989).

By looking at the observed  $H\alpha$ -line profiles reported in paper 1 (Zharkov et al. 2020) we recognised that in kernels 2 and 3 the profiles are clear blue wings, a far wing in kernel 2 and a near wing in kernel 3. In kernel 1 the observed  $H\alpha$  line profile can be considered at first to be the regular profile with self-

absorption and strongly increased red horn in the line core reported previously for near stationary and slightly moving atmospheres (Ding & Fang 1996; Kuridze et al. 2015; Druett et al. 2017). However, it turns out that this is not the case because of the very strong intensity of the whole emission and, particularly, of the red wing of the profile, which is higher than the  $H\alpha$  line profiles even in the cores simulated for weaker beams. Furthermore, the observed  $H\alpha$  line intensity in kernel 1 is still increasing as it reaches the edge of the available wavelength window ( $+1.5 \text{ \AA}$ ). However, based on the features present in the observation profile, it is certainly likely that we observed the near blue wing of the line since the line may not be so greatly red-shifted as is in kernels 2 and 3.

For these reasons we calculated  $H\alpha$ -line profiles produced from hydrogen atoms by combined thermal and non-thermal excitation and ionisation by beam electrons in flaring atmospheres heated by: 1) mixed beam with the initial energy flux of  $1.0 \times 10^{13} \text{ erg}\cdot\text{cm}^{-2}\cdot\text{s}^{-1}$  (model F13), spectral index 4 as derived for the flaring events 1 and 2 in paper 1 (Zharkov et al. 2020), and 2) by electron beams with much smaller initial energy fluxes of  $1.0 \times 10^{11} \text{ erg}\cdot\text{cm}^{-2}\cdot\text{s}^{-1}$  (model F11) and  $1.0 \times 10^{10} \text{ erg}\cdot\text{cm}^{-2}\cdot\text{s}^{-1}$  (model F10) for the spectral index of 4, in case if the electron component in the mixed beam in kernel 1 was much smaller than in kernels 2 and 3. Interestingly, none of the simulated  $H\alpha$  line profiles do not show self-absorption in the line cores unlike reported earlier in weaker flares (Kuridze et al. 2015; Druett et al. 2017) that is likely to be defined by strong non-thermal ionisation of hydrogen atoms. This, in turn, reduces the number of neutral hydrogen and thus, optical thickness in  $H\alpha$  lines that makes line profiles without self-absorption.

It can be seen that the simulated  $H\alpha$  line profiles for any HD model shown in Fig. 5 are mainly dominated by the downward motion of the hydrodynamic shocks shown in Fig. 3 generated in response to the injection of beam electrons with different fluxes or to the injection of mixed beams with electrons (shown in Fig. 2c). Depending on the shock velocity varying from 40 to 380 km/s, the red shifts in  $H\alpha$ -line profiles can vary from 1–2 Å (5a), or 3–4 Å (5b) or to >5 Å (5c and 5d) often observed in the past in the other flaring events with spectral windows of  $\pm 8$  Å (Ichimoto & Kurokawa 1984; Wuelser & Marti 1989).

The  $H\alpha$  line profiles simulated for the green rope footpoints in kernels 1 and 2 of flaring event 1 are based on the hydrodynamic models simulated for a mixed power-law particle beam F13 (see Fig. 2, left column) in the flaring atmosphere associated with the seismic source 1 (footpoint FP3 in the northern end of green rope in Fig. 1) and with the seismic source 2 (footpoint FP4 in the southern end of green rope) as concluded in Paper 1. Since this KONUS observation does not have a spatial resolution, we can only rely on the observed kernels of  $H\alpha$  emission and seismic signatures in the kernel locations for the evaluation of the parameters of particle beams producing their emission co-temporally with HXR emission (see sections 2.2 and 2.4). The total energy flux of the high energy emission observed by KONUS in the areas of  $H\alpha$  kernels 1 and 2 was between  $(8 - 12) \cdot 10^{12} \text{ erg}/\text{cm}^2/\text{s}$  (or model F13) as derived in Paper 1.

Since these estimations of the initial energy fluxes of the beams in flaring atmospheres from the areas of  $H\alpha$  kernels are not derived directly from the HXR observations located in the kernels as well, but on some assumptions how the total beam energy was redistributed between a few footpoints where the SQs and  $H\alpha$  kernels occurred, one can only estimate the order of magnitude of the initial energy flux of particle beams while the exact coefficients in front of the order of magnitude can be flexible as they are somehow dependent on the assumptions. Therefore, we simplify the interpretation by considering only the basic initial energy flux F13 and discuss possible deviations of the simulated profiles from the observed ones in particular kernels.

The  $H\alpha$ -line profiles derived at kernels 1–3 are plotted in different colours on the top of model simulations of these profiles calculated for the atmosphere heating by beams with the initial energy fluxes relevant to models F10, F11 and F13 as shown in Fig. 5. It can be seen that the observed blue wings of  $H\alpha$  line profiles in all three  $H\alpha$  kernels only fit the model F13 at the times of 5 s (kernel 1) and 15 seconds (kernels 2 and 3), while the observed  $H\alpha$  blue wing intensities were much higher than those simulated for the HD models heated by the beams with lower energy fluxes (F10 or F11). The vertical lines show the spectral window of CRISP/SST which demonstrate the limits of the observations of  $H\alpha$  line profiles with the largely red-shifted cores.

The  $H\alpha$ -kernel 2, which occurred from 11:55:50 UT during the flaring event 1, is associated with seismic source 2. The red shift in the simulated  $H\alpha$  line profile of kernel 2 reaches a maximum of above 5–6 Å at 5 s, or just after a beam offset, when the downward velocity in a hydrodynamic model is maximal approaching  $380 \text{ km}\cdot\text{s}^{-1}$  dropping below 300 km/s after 15 seconds (see Fig. 2c, right plot or Fig. 3a.) The simulated  $H\alpha$  line profile is found to be strongly red-shifted by more than 5.0 Å from the central wavelength ( $\lambda = 6563$  Å), corresponding to an averaged Doppler velocity of  $268 \text{ km}\cdot\text{s}^{-1}$ . The core of this  $H\alpha$  line profile cannot be observed by CRISP because it is strongly red-shifted far outside the CRISP spectral window of  $\pm 1.5$  Å.

As result, we reckon the observed  $H\alpha$ -line profiles in the spectral window of  $\pm 1.5$  Å shows only far blue wings of the  $H\alpha$  line, because the line is strongly red-shifted by the shock induced by a mixed beam with the high initial energy flux. Hence, the observed  $H\alpha$ -line profiles in kernel 2 is close to the simulations made for the F13 model about 15 seconds after the beam onset as shown in Fig. 5d with much lower intensity of this blue wing. For possible observation of  $H\alpha$  emission by CRISP in powerful flares there should either usage of a fast shift of the spectral window to the red wing of the line, or to observe the  $H\alpha$  line profiles a minute or so later after the flare onset. While for the  $H\alpha$  kernel 1 the blue wing fits better the line profile at 5 s after the beam onset that might signal the timing when the beam in this flaring atmosphere reaches the footpoint FP3 where this kernel was measured.

The  $H\alpha$ -kernel 3 observed at 12:06:48 UT in the flaring event 2, occurred about 10 minutes later after the flaring event 1. It was located close to the seismic source 2, so that the seismic signatures in this location should become overlapped. It fits rather well the simulated  $H\alpha$  line profile calculated for the model F13 (see Fig. 5c). The second flaring event was observed only by Ly $\alpha$  and GOES emission and by  $H\alpha$  emission with high spatial resolution of CRISP instrument. 1.2 minutes after this event there were HXR observations by RHESSI with the contours located exactly in the location of the  $H\alpha$  kernel 3 shown in Paper 1. In the absence of HXR emission for this event we can only speculate that the same magnetic configuration has produced a sympathetic flaring event after FE2 and accelerated particles to power law beams with the close parameters as in FE2. By comparing the observed  $H\alpha$  line profile in kernel 3 with the simulated ones shown in Fig. 5, we reckon that this footpoint F4 was heated by a powerful mixed beam with the

initial energy flux about or above  $(6 - 8) \cdot 10^{12} \text{ erg}\cdot\text{cm}^{-2}\text{s}^{-1}$  (still of the same order of magnitude as in  $H\alpha$  kernels 1 and 2).

This shock in the flaring event 2 should produce a noticeable seismic response in the seismic source 5, which can be comparable with that observed in the flaring event 1 occurred 10 minutes before in the seismic source 2. However, this seismic event 5 is obscured by the ripples from the seismic events 2 and 3, thus, cannot be detected by either methods of sunquake detection.

### 3.3. Simulated Paschen continuum (WL) emission

The temporal variations of white light emission at the WL locations in the  $H\alpha$  line kernels 1 and 3 observed from WL images from the HMI/SDO instrument can be also compared with the simulated temporal profiles in the Paschen continuum of hydrogen atoms obtained using non-LTE simulations. It was shown by (Druett & Zharkova 2018) that Paschen continuum originates in the chromosphere and photosphere, and the beam electrons are the main agents producing Paschen continuous emission, which is seen as white light emission. The contribution functions for Paschen continuum responsible for white light emission are presented in Paper 1 assuming that in WL kernel 1 ( $H\alpha$  kernel 1) the emission is produced by the beam with initial energy flux of  $(4 - 5) \times 10^{10}$  (F10) and the WL kernel 2 ( $H\alpha$  kernel 3) the WL emission is produced by the beam with the energy flux of  $10^{13}$  (F13).

This WL emission occurs owing to strong ionisation and excitation by non-thermal electrons which enhance Paschen continuum contributions at all atmospheric levels (Druett & Zharkova 2018). It is important to note that, with the injection of powerful beam electrons and the non-thermal ionisation by them of hydrogen atoms, the Paschen continuous emission is produced not only in the photosphere, as happens in the quiet sun, but mostly in the chromosphere, as the left plot of Fig. 6 undoubtedly show for moderate beam. While the more powerful beam produces much stronger (order of magnitude) Paschen continuum emission in the photosphere than in the chromosphere. Evidently, beam electrons are the agents producing the main contribution for white light flares (Druett et al. 2017; Druett & Zharkova 2018), in general, and for this particular event on 6 September 2017.

Now by looking at the contribution functions of Paschen continuum produced by the beams F10 and F13 one can note that the intensity of this emission for the F13 beam is more than an order of magnitude higher than for the model F10. This is governed by a large opacity of Lyman continuum emission in F13 model (Druett & Zharkova 2019), which increases the intensity of all hydrogen continuum emission. In particular, Paschen continuum emission for the F13 beam is formed at deeper atmospheric levels and has much longer existence compared to that induced by less powerful beam of the model F10. Since the observations confirm the very intense and long-lasting white light emission of the flare of 6 September 2017 combined with the fit of  $H\alpha$  line profiles in the kernels for FE1 and FE2, we can confirm that the optical emission in this flare was produced by a very intense beam.

The emission in the first WL kernel (Fig. 6c) is likely to be caused by a weak beam as derived from kernel 1 of  $H\alpha$  emission in section 3.2, whose line profile is likely produced by the rather weak beam. While the second white light kernel 2 (Fig. 6d) was co-spatial to the  $H\alpha$  kernel 3 in flaring event 2 associated with a much stronger electron beam injected after 12:06:40 UT. The electron beam in the flaring event 2 produces stronger ionisation of the ambient hydrogen and stronger Lyman continuum, which controls the continuous hydrogen emission in flaring atmosphere, affecting, in turn, the intensity and duration of the Balmer and Paschen continua via the opacity of Lyman continuum (Druett & Zharkova 2019).

This logically explains a much slower decrease of the observed white light emission in the second WL kernel (Fig. 6d) compared to the first one (Fig. 6c). Moreover, it looks like in the WL kernel 2 there were two beam injections following  $Ly\alpha$  light curves shown in Paper 1 (Zharkov et al. 2020) that is revealed in the WL emission by a double maximum. This may explain the very extended decay of WL emission in this flaring event that is also confirmed by other observers (see, for example Romano et al. 2018).

## 4. Hydrodynamic response of the solar interior

### 4.1. Theory of acoustic response of the solar interior

Hydrodynamic shocks from the flaring atmosphere discussed above in section 2 can be used as the initial condition for another hydrodynamic model developed for acoustic wave propagation in the solar interior (Zharkov 2013). Since the atmospheric hydrodynamic shocks can travel in the solar interior with supersonic velocities they generate acoustic (or magneto-acoustic) waves owing to another hydrodynamic response, this time of the solar interior to the shock. As was shown by Zharkov (2013) the vertical shock perturbation moving with a supersonic velocity can generate the set of multiple acoustic waves, from which only the waves with the phase speed exceeding a certain threshold (see Equation 5.8 in Zharkov 2013) can produce the observable acoustic waves. Using Lamb's acoustic cut-off frequency and the sound speed profile from a solar interior mode, the acoustic wave equation can then be solved either analytically for a polytrope model of the solar interior (Zharkov 2013) or numerically (Shelyag et al. 2009) for Christensen-Dalsgaard's model S (Christensen-Dalsgaard et al. 1996) as described by Macrae et al. (2018).

The source of the deposited impulse, depending on its properties, generates a family of the rays that provides the solution to the ray equations in phase space and defines the generated wave front. The waves generated by the initial shock are contained in a closed cone around the velocity vector propagating in the solar interior. Zharkov (2013) evaluated for a polytrope model the parameters of generated acoustic wave packets and the condition of their detection from Doppler observations. Because the source generating the waves is located in the interior, the first ray (out of all generated by the source) to reach its upper turning point defines the minimal distance where the ripple is formed. An individual ray, characterised by constant fre-

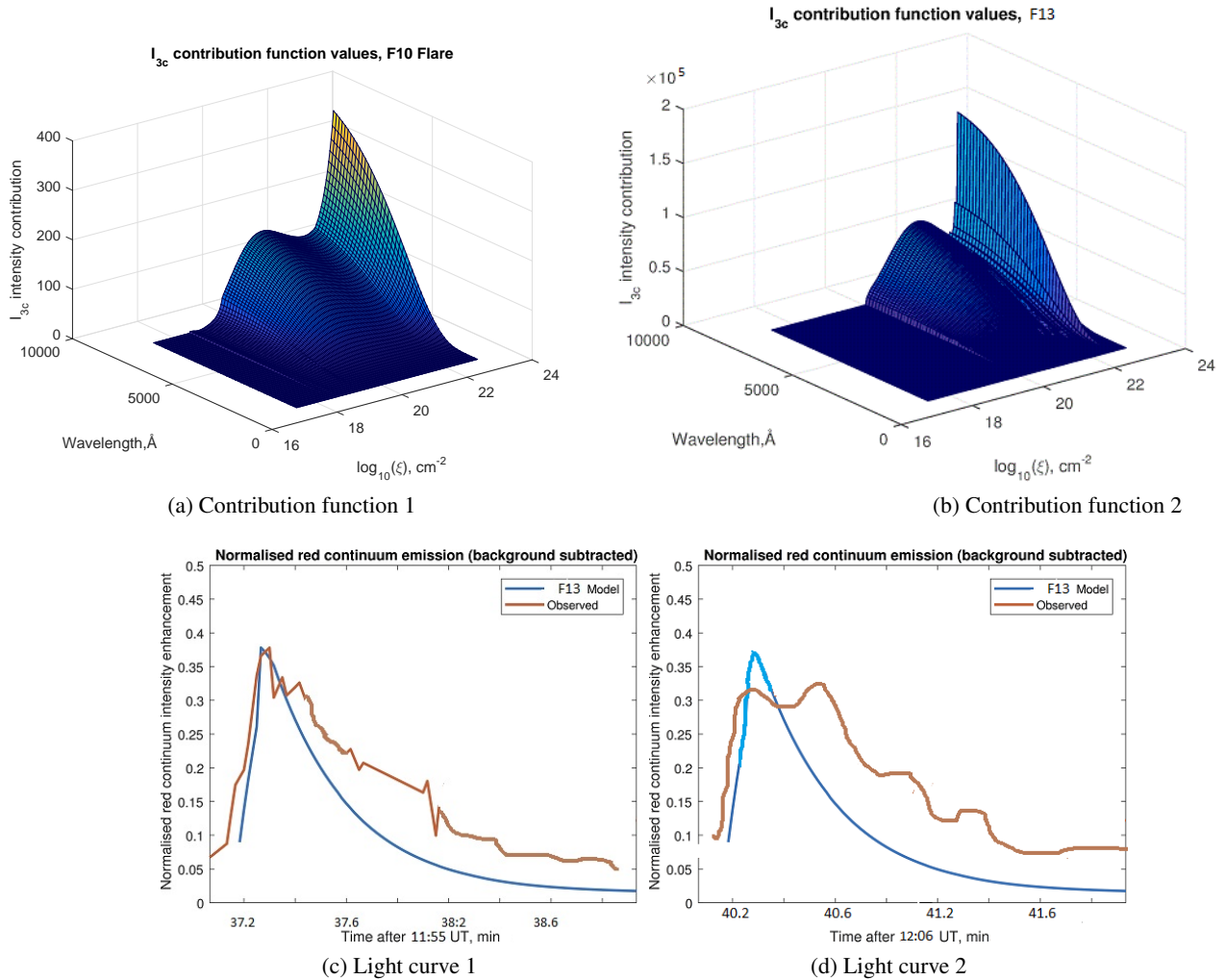


**Fig. 6.** Simulated variations of the contribution functions of Paschen continuum (white light emission) derived from a radiative hydrodynamic model heated by the moderate electrons beam, model F10 (a) and by powerful mixed beam, model F13 (b) (see the text for more detail). Note the three orders of magnitude difference between the intensities in the model (F10) and (F13) plots. The comparison of the light curve of intensity of Paschen emission generated by a mixed beam with spectral index of 4 and the initial energy flux of  $1 \times 10^{13} \text{ erg/cm}^2/\text{s}$  with that measured from HMI/SDO images in the WL kernel 1 coinciding with H $\alpha$  kernel 1 (c) and in the WL kernel 2 coinciding with H $\alpha$  kernel 3 (d).

quency,  $\omega$ , and horizontal wavenumber,  $k_h$ , initialised at given depth, generally will have two, upper and lower, turning points (see Fig. 1 in Zharkov 2013). The first upper turning point along the ray defines its first surface appearance (as a first ripple), the lower turning point indicates where the wave changes its direction of its motion in the interior by being reflected back to the surface. Then the propagating ripples correspond to a sequence of the source-generated acoustic rays from the packet reaching in succession their upper turning points (for more details see also Macrae et al. 2018).

For a near-surface source, the first surface appearance of reflected wave, or the minimal distance from the deposition point, can be approximated by the ray's skip distance,  $\Delta$ . For the polytrope model of the solar interior (Zharkov 2013) the minimal skip distance,  $\Delta$ , or the distance from the point of the initial impulse deposition to the first ripple occurrence (see the Appendix A1 in Zharkov 2013) as follows:

$$\Delta(k_h, \omega) = (\omega)^2 \pi m / (k_h)^2 g = (V_{ph})^2 \pi m / g, \quad (1)$$

where  $g$  is the gravitational constant,  $g = 2.67 \times 10^{-4} \text{ Mm s}^{-2}$ ,  $m$  is the polytrope index,  $V_{ph} = w/k_h$  is the horizontal speed of wave propagation.

In this case, the rays are generated with varying frequencies above the acoustic cut-off frequency  $\omega_{ac}$  at the source depth (Zharkov 2013; Macrae et al. 2018). The observations of high-frequency waves will be also limited by the Nyquist frequency,  $\omega_N$ , of a given instrument (11.11 mHz for HMI/SDO) and cadence of the series, e.g. the acoustic waves with a frequency above Nyquist frequency may not be observed.

Hence, a threshold for the minimal phase speed,  $v_{ph}^{min}$ , defining the condition for registering the first ripples on the surface by the following relation (see Equation (5.8) in paper Zharkov 2013)) can be written as:

$$v_{ph}^{min} = \frac{vc}{\sqrt{(1 - \frac{\omega_{ac}^2}{\omega_N^2})v^2 - c^2}}, \quad (2)$$

where  $c$  is the sound velocity,  $v$  is the acoustic wave velocity.

The propagation of the surface ripples from a near-surface source can be determined by the phase speed of acoustic waves (Zharkov 2013), the minimal skip distance,  $\Delta$ , can be estimated from Eq. (1) after a substitution of the minimal phase speed given in Eq. (2). The minimal skip distance is where these acoustic waves are reflected by the surface (the upper turning point) and observed as surface ripples.

Therefore, in order to interpret the observed seismic responses for this flare we need to establish the following points: 1) what was the depth in the solar interior where the atmospheric shock is deposited; 2) what was an average velocity of the shock; 3) for how long this velocity exceeded the local sound speed in the solar interior; 4) how deep the generated acoustic waves propagate into the solar interior, or how deep was their lower turning points; 5) with what speed the acoustic waves will travel back to the surface after their reflection in the lower turning point; 6) at what distance from the flare location is the upper turning point; 7) what is a height of the ripples in the upper turning point, where the waves are reflected

from the photosphere back to the solar interior. The answers to these points will define if these acoustic waves are detectable and how they are detectable: either as ripples or as holographic images only.

## 4.2. Sunquake properties probed by the acoustic response models

Hydrodynamic modelling in a flaring atmosphere discussed in section 2.4. These beam-generated shocks entering the sub-photospheric layers at a supersonic speed as shown in Fig. 7, can generate acoustic waves (Zharkov 2013), which can be seen on the solar surface, or photosphere. The acoustic waves generated in the interior are determined by the interior plasma properties at specific depths (e.g. sound speed, acoustic cut-off frequency), as well as by the shock velocity and its angle of shock propagation towards the normal to the surface.

### 4.2.1. Observed properties of the sunquakes

Let us summarise the expected shock parameters associated with the detected seismic sources as follows. The three sunquakes (SQs) 1, 2 and 3 reported in Paper 1 appear at 11:55:37 UT during the flaring event 1. According to the shape of H $\alpha$ -line profile in kernel 1 observed in this location, and the speed developed by ripples in the seismic source 1 can be referred to the shock induced by a strong electron or mixed beam with the energy flux about  $(6 - 8) \times 10^{12} \text{ erg} \cdot \text{cm}^{-2} \text{ s}^{-1}$ , while for the SQs 2 and 3, as concluded from the shape of H $\alpha$  line profiles and the ripples speed, one have to assume the shocks induced by very powerful mixed beams with the initial energy flux of  $(8 - 12) \times 10^{12} \text{ erg} \cdot \text{cm}^{-2} \text{ s}^{-1}$ . All three SQs were detected with the holography method and time-distance diagrams.

The first signs of ridge in TD diagram for this SQ 1 appear 20-25 minutes after the flaring event onset. Also the angle of shock deposition is about  $-0^\circ$  from the local vertical according to the directional holography image. The ripples generated by the shock in seismic source 1 approach the distance of 120 Mm with a velocity of 48 km/s. The seismic source 3 has a faster phase speed of the ripples propagation because its ridge is sharper and approaches the distance of 120 Mm faster with a speed of 51 km/s.

The strongest sunquake, SQ 2, which occurred simultaneously with gamma-ray emission and H $\alpha$  kernel 2 reported in Paper 1, is well detected in the TD diagram with two ridges revealing for the first time the observations of the first and second bounces (upper turning points) of acoustic waves from the solar surface. The TD diagram for seismic source 2 shows an initial phase velocity of the ripples on the photosphere of 35 km/s approaching 53 km/s at the edge of the 120 Mm data cube. The first bounce occurring at 11:55:37 UT at 5-10 Mm from the flaring event location, where the first ripples were observed, is closer than any other sunquakes observed before that was also noted by other authors (Zhao & Chen 2018; Sharykin & Kosovichev 2018).

The HD simulations for F13 model show that downward macrovelocity of the shock (see Fig.7, left column plots) for the

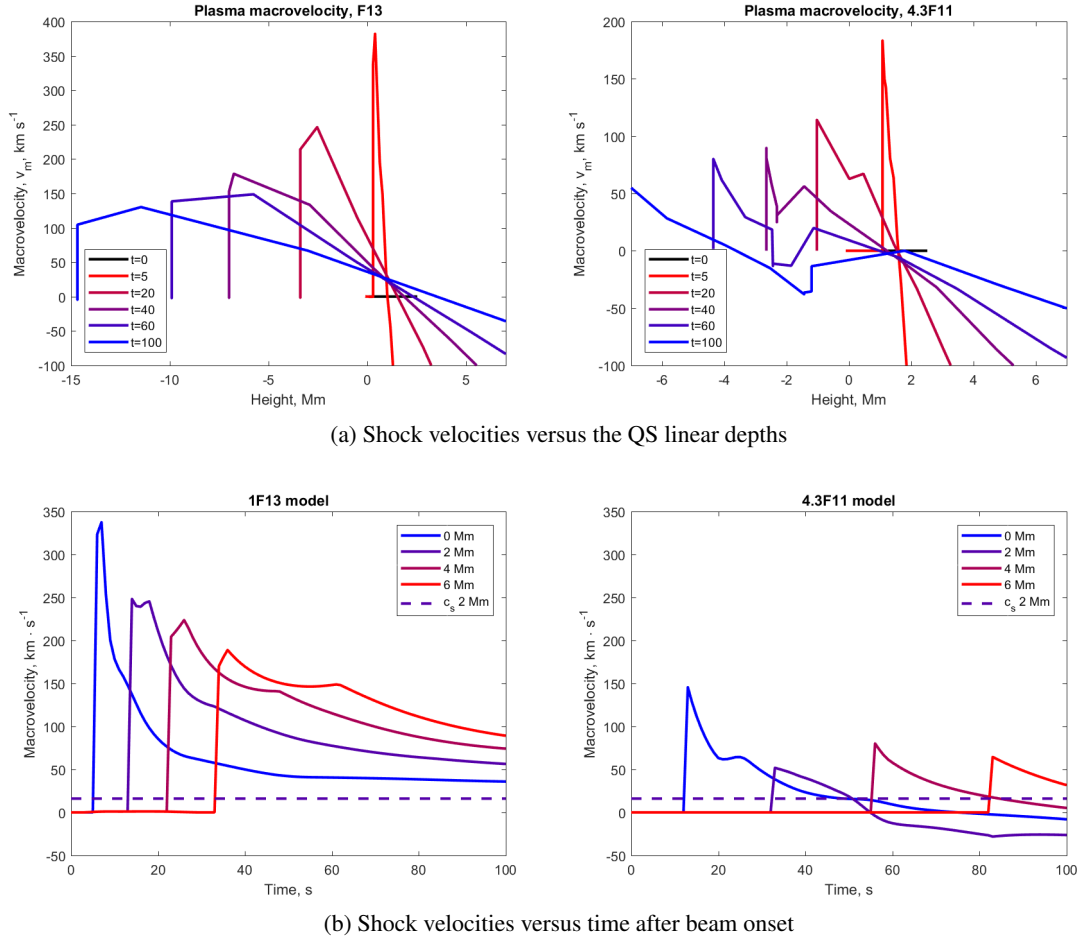


**Fig. 7.** Velocity profiles of the simulated hydrodynamic shocks in the seismic event 1 (left column) and 3 (right column) plotted versus linear depths under the quiet Sun (QS) photosphere for different times after beam injection (top row) and versus time after the beam onset for different linear depths in the solar interior under the QS photosphere (bottom row). Zero in the X-axis indicate the position of the QS photosphere, the negative numbers indicate the depth under the photosphere (see text for details). The solid black line in (a) represents sound speed in the photosphere.

conditions close to SQ 1-3 approaches 380 km/s at the maximum flux of the injected beam, while the average velocity over first 50 seconds is about 180-200 km/s. The plasma density of the shock induced by the mixed beam with the given initial energy flux varies as  $(2 - 6) \times 10^{13} \text{ cm}^{-3}$ . For comparison, the conditions of a shock produced by the electron beam with the initial energy flux of  $4.3 \cdot 10^{11} \text{ erg} \cdot \text{cm}^{-2} \text{ s}^{-1}$ , which was derived for the flare of 6 September 2011 (Macrae et al. 2018) is presented in Fig. 7, right column plots. The shock induced by the less intense beam reaches the velocities of 250 km/s at 5 seconds after the beam onset with the average velocity not exceeding 120-150 km/s. The ripples induced by the flare of 2011 were much smaller than in the current flare of 2017, so that the ridge in the TD diagram in the flare of 2011 was even missed until Macrae et al. (2018) managed to apply the improved holography and TD techniques allowing the authors to detect the missing sunquake.

The shocks generated by a mixed beam shown in Fig. 2c, left plot are presented versus a linear depth of the quiet Sun (a) and time (b) (see Fig. 7, left column) while the shocks deposited by an electron beam are shown in Fig. 7, right column.

It can be noted that the shocks generated by the electron beam were first deposited above the solar surface and only later propagated with a supersonic velocity into the solar interior to the depths above 500 km. Since the shocks travelled not a very long distance in the interior, it did not produce very intense acoustic waves, so that the ridge they produced in TD diagram is not very deep that explains why it was missed at first.

While the shock produced by the mixed beam shown in Fig. 7, left column) is deposited from the very first seconds in the solar interior with a supersonic speed. The hydrodynamic shock formed in a flaring atmosphere enters the solar interior (crosses the linear depth of zero) above the local sound speed, with the vertical velocities of  $v(z_s) = 380 \text{ km} \cdot \text{s}^{-1}$  at  $z_s = 100 \text{ km} \cdot \text{s}^{-1}$  (Fig. 7a). The density of the shock should be  $(1 - 3) \times 10^{13} \text{ cm}^{-3}$ . The macrovelocities of a downward moving hydrodynamic shock reach  $280 \text{ km} \cdot \text{s}^{-1}$  at 5 s then slowly reducing to 175 at 50 s, approaching 100 km/s at 100 s, so the average macrovelocity is about  $180\text{-}200 \text{ km} \cdot \text{s}^{-1}$  (see Fig. 7, left column). These downward velocities were complied well with those derived from the  $H\alpha$  kernels 1 and 2 detected in the locations of seismic sources 1 and 2 for the flaring event 1.



The depth of deposition of this shock in these events starts from the surface, or quiet sun photosphere, and moves down to 1000 km depth in the interior. The plasma density in the shock is about  $(5 - 6) \times 10^{13} \text{ cm}^{-3}$ . Thus, such the shock is capable of producing intense acoustic waves for a rather long time while travelling inside this interior (compare the curves for different times in Fig. 7a.) Hence, the shock produced by the mixed beam produced a very deep ridge for the first bounce. And because the first set of acoustic waves was very intense, they had enough energy to travel to the interior, be reflected from it back to the surface following the Fermat principle and to travel to the solar surface again to become bounced back by the photosphere at the second upper turning point, as the theory predicts. Only very intense mixed beam can produce such the phenomenon observed for the first time for the flare 6 September 2017 (Zharkov et al. 2020).

The difference in the velocities of ripples at the edge of the dataset of 120 Mm in sunquakes 1, 2 and 3 explains a slight difference in the real flux of the mixed beams, which generated the shock in SQ1 (the lowest initial energy flux, SQ3 (medium flux) and SQ2 (the strongest initial energy flux). Also the fact that in SQ2 a ridge appears at about 10 minutes after the event onset, or at 5-10 Mm from the location of the flaring event 1 onset indicate that the shock in SQ2 was deposited under larger angle to the local vertical, which from the directional holography is found to be of  $-30^\circ$ . The directional holographic image for SQ 3 also indicates the inclination of the shock at about  $+30^\circ$  from the vertical to the surface. The SQ1 is found to have the shock deposited closely along the local vertical under the angle of  $0^\circ$ .

The most southern seismic source 4 and middle seismic source 5 appear between 12:04 -12:07 UT according to Ly $\alpha$  light curve with FE2 starting with H $\alpha$  kernel 3 at 12:06:48 UT. We do not have any high energy observations besides UV light curve in Ly $\alpha$  line. Hence, the energy flux of a beam causing the shocks in these two seismic events is a big question. However, it looks like there was a repeated injection of a strong electron beam happened in the same location 10 minutes after the injection of the first mixed beam. This injection is likely caused another strong hydrodynamic shock and led to a potential (repeated) seismic source 5. Hence, in the flaring event 2 there was another H $\alpha$  line kernel 3 with a large red shift detected in the same location as seismic source 2.

By comparing the line profile observed in H $\alpha$  kernel 3 we managed to derive that it can be produced in flaring atmosphere heated by a mixed beam with the initial energy flux close to  $(6 - 8) \times 10^{12} \text{ erg/cm}^2/\text{s}$ , spectral index is 4. From the simulated hydrodynamic model we derive that the density of the shock should be  $(1 - 3) \times 10^{13} \text{ cm}^{-3}$ , and the shock macrovelocity would be slightly lower than in source 2 reaching 320  $\text{km s}^{-1}$  at 5-10 sec and dropping to 100 at 50-60 s, with the average velocity of 120-140  $\text{km s}^{-1}$ . The shock starts above the surface and propagates as a shock down to 500-1000 km below the surface, and the angle of deposition is about  $+30^\circ$  from the vertical as derived from directional holography approach.

It is likely that the ripples generated by this hypothetical seismic source 5 can be interfering with the ripples from this seismic source 2 generated before in the same location. These

acoustic waves can have a resonant interference once suggested for the similar seismic events seen in Ca II dopplergrams by Hinode (Kosovichev 2011), thus producing the unusual seismic waves observed in Ca II emission in the chromosphere (Quinn et al. 2019).

For acoustic-wave propagation modelling Christensen-Dalsgaard Model C (Christensen-Dalsgaard et al. 1996) is used with the source parameters described above. The profiles of the acoustic cutoff frequency and sound speed in this model are shown in Macrae et al. (2018). The acoustic cut-off frequency,  $\omega_{ac}/(2\pi)$ , and sound speed,  $c$ , at the depths below the surface less than 1000 km are accepted to be equal to 9.9 mHz and 8.4  $\text{km s}^{-1}$ , respectively. In addition, in the simulations for different seismic sources we introduced inclinations of  $\pm 30^\circ$  to the local vertical of the direction of a deposited hydrodynamic shock.

#### 4.2.2. Simulated acoustic waves versus observations

Propagation of the acoustic waves (or rays) generated by a supersonic source moving with velocity 150  $\text{km s}^{-1}$  under the angle of  $0^\circ$  to the vertical (seismic source 1) is shown in Fig. 8, and with average velocity of 150  $\text{km s}^{-1}$  under the angle of  $+30^\circ$  in Fig. 9 and with the average velocity 200  $\text{km s}^{-1}$  at surface depth  $z_s = 0 \text{ km}$  (as in seismic source 2) under the angle of  $-30^\circ$  in Fig. 10. The abscissa defines a horizontal distance in Mm of the ray propagation about the location of a deposition of supersonic disturbance (shock) and the ordinate shows a propagation depth,  $z$ , under the photosphere of the generated rays and wavefronts at different times are shown in Figs. 8 and 10 for the wave vectors located in the same plane as velocity, i.e. if  $\phi = 0$  (in notation of Section 5.2 of Zharkov 2013).

The acoustic wave simulation for the conditions of seismic source 1 show (see Fig. 8) that the rays in the first model deposited nearly along the local vertical have propagation of the waves in the interior (left plot) until the first ripple is observed at 15-20 Mm from the location 20-25 minutes after the shock deposition (right plot). Since the rays move in the interior with a speed exceeding the local sound speed, these waves at frequencies above the acoustic cut-off can escape the solar interior. when they reach a surface at the upper turning point. As we noted from the HD simulations of the shock deposition (Fig. 7a, right plot) in this source, the shock goes under the photosphere 10 s after the event onset. Then after 20. minutes the rays in the model simulations shown in Fig. 8 reach the first upper turning point at the surface in the photosphere where they produce the first ripples on the surface before they turn back toward to the interior.

For a shock deposition applicable for seismic event 3 the appearance of the ridge is seen earlier at 10 seconds and at the distance of 8-10 Mm (Fig. 9). This happens because the deposition angle of the shock in source 3 was not zero but  $+30^\circ$ , e.g. the rays on the left from the deposition point travel less deep into the interior and thus reach the surface faster than in the source 1 at 16.83 minutes. The left rays in source 3 travel



deep enough but they produce the ripples too far away from the source, outside the data cube of 120 Mm.

While for the seismic model for SQ 2 shown in Fig. 10, the shock caused by the mixed beam is deposited at the surface and propagates much deeper into the interior (as shown in the video attached with the paper in supplementary materials) so that the acoustic wave produced by this shock moves into much deeper interior now under the angle  $-30^\circ$  producing acoustic rays in the shortest path on the right hand side and the longest one on the left hand side. Since the acoustic rays travel much deeper into the interior, they gain much higher velocity before reaching the lower turning points than in the previous case described above. These rays when reflected back to the surface by Fermat principle (Zharkov 2013) will have much higher velocities and, when they approach the photosphere in the upper turning point, they create larger ripples, which can be easily detected in the time-distance diagrams as reported for seismic source 2 shown in Paper 1.

Because the shock is deposited at an angle of  $-30^\circ$  from the local vertical, the first upper turning point is seen very quickly at about 8–10 minutes after the impact at the distance approaching 5 Mm from the source. This is in close agreement with the skip distance derived from TD diagrams and similar to the results reported by Zhao & Chen (2018). Moreover, for this seismic event the velocities of the rays reflected back to the interior after they produced the first ripples are still high. This is reproduced in the model acoustic waves shown in Fig. 10, where the first points of reflection from the surface are observed at 15 minutes after the deposition time starting from a distance 2 Mm and very well seen in 20 minutes from the distance 3 Mm.

Since the shock deposited in atmosphere with SQ2 was very strong, these reflected rays are capable to travel again to the interior and back. Given the high ratio of the source-to-local sound speed, the wave-packet generated at this depth is expected to be rather wide because only the rays with  $\theta > 86^\circ$  become evanescent for  $\phi = 180^\circ$ . Hence, as result, these acoustic waves are rather strong to produce the second lower and upper turning points leading to a second bounce seen in TD diagram for this seismic source reported in paper 1 (Zharkov et al. 2020). Indeed, these second bounce waves are seen in the simulated acoustic waves shown in Fig. 10 (the top right end of the wave set marked by the blue curve) showing the second bounce waves to start at 5 Mm in the model set at 15 minutes and at 7 Mm in the set at 20 minutes.

When the shocks in any models travel deeper into the interior, their velocity decreases while the sound speed grows making the wave packets generated at these larger depths narrower and with lower frequencies. The fact that for the seismic events 2 and 3 there are observed signatures at low frequencies of 3 mHz indicates that the shocks generated in these events must have travelled to at least 600–1000 km below the surface, which is in agreement with the modelling of hydrodynamics of flaring atmosphere. While the seismic event 1 was generated in a shallow region below the surface and does not reveal lower frequency acoustic waves.

Hence, in the summary, one can note that the acoustic waves (rays) generated by hydrodynamic shocks induced by a mixed beam (MB) in the largest sunquake (source 2) are

found to travel much faster and to deposit their momentum much deeper in the solar interior producing acoustic waves of type 1 with double ridges: a very visible main ridge and a detectable second-bounce ridge. The shocks deposited by an electron beam (EB) produce acoustic waves of type 2 with a weaker single ridge as seen in the seismic sources 1 and 3. As a result, these acoustic waves of type 1 reach the first lower turning point in deeper interior depths, thus, gaining higher velocities compared to the waves of type 2. These type 1 acoustic waves approach higher velocities in the interior, with which they travel back to the surface in the photosphere to their first upper turning point (or first bounce) creating ripples while being reflected back to the interior. The reflected wave energy is lower than the original one but sufficient to travel again to the less deep interior and to return back for a second bounce creating secondary, slower, ripples.

From a directional holography analysis, the different seismic sources are found to have different directivity, or angle from the vertical for a momentum deposition. The acoustic waves of type 1 simulated in the seismic source 2 for a momentum deposited at an angle of  $-30^\circ$  from the vertical demonstrate the occurrence of well detectable ripples at the photosphere seen a few minutes after the impact at a distance approaching 5–10 Mm from the source that is in a close agreement with the distance derived from the TD diagram.

The other two sources show the rays characteristics consistent with being produced by shocks generated by electron beams and deposited at angles  $(0-10)^\circ$  (source 1) and  $+30^\circ$  (source 3) to the local vertical, which propagate beneath the surface but not too deep into the interior, contrary to type 1 acoustic waves in seismic source 2. These weaker shocks create weaker acoustic waves at shallower depths of the interior, which are reflected by the interior to the solar surface (at lower turning points) with smaller velocities. When these acoustic waves reach the solar surface (photosphere) and become reflected by it (at the upper turning point), they create much smaller ripples in the photosphere, which can be only picked up as regular features by the holographic approach.

## 5. Discussion and conclusions

In this paper 2 we attempt to understand the complex appearance of two flaring events in the flare of 6 September 2017, which were observed with a different degree of coverage in time and space by multi-wavelength instruments. During the flare there were four locations linked to footpoints of three magnetic ropes where 4 (5) sunquakes are identified with acoustic holography (4) and time-distance diagram (3) techniques. There were also three  $H\alpha$  kernels observed: the two during FE1 with strongly red-shifted line profiles co-spatial with 2 detected sunquakes (SQ1 and SQ2) and the one kernel during FE2 linked to the alleged SQ5 occurred during FE2 in the location of SQ2 10 minutes later after FE1. The locations of sunquakes 1–3 of FE1 were overlapped with strong EUV emission reflecting explosive evaporation of the chromospheric plasma into the flaring corona in these locations observed by EIS/Hinode, whose field of view could not see the SQ4 in the southern part of the active region. There were also the loca-

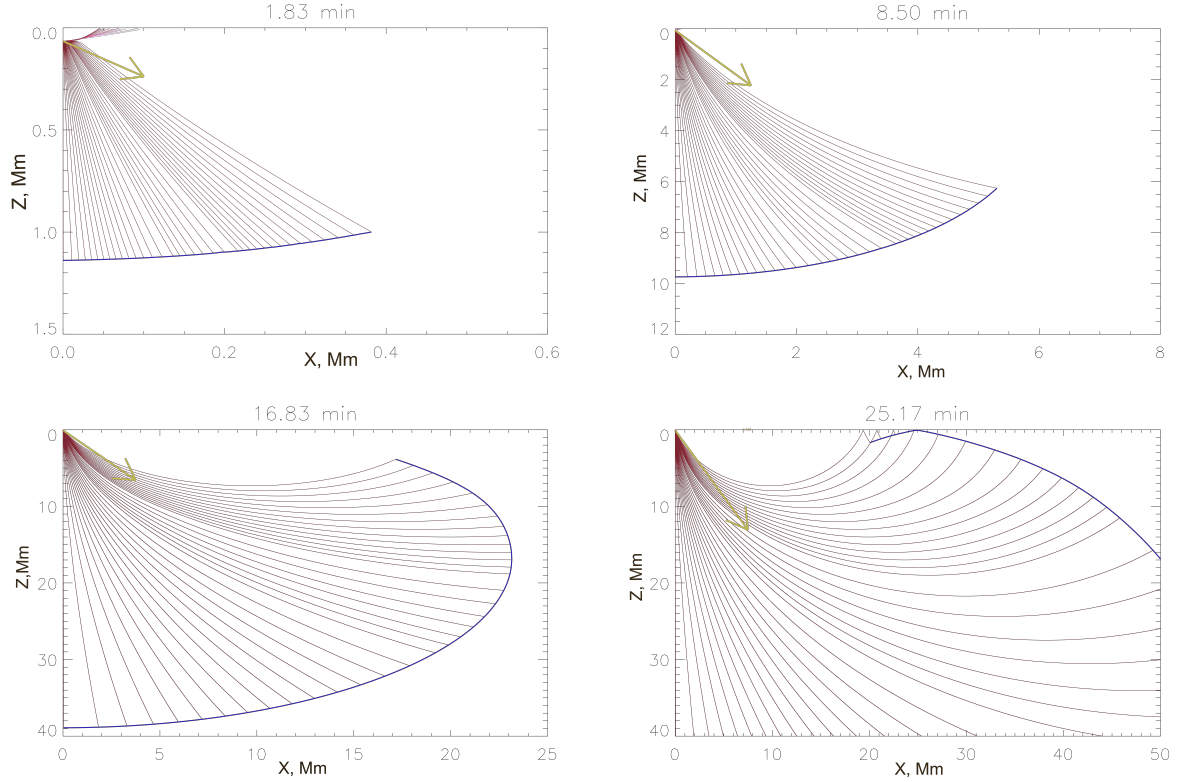


**Fig. 8.** The individual acoustic rays generated at the depth of 1 km in the solar interior and travelling along  $Z$  direction to the bottom of the plot by a moving supersonic source,  $v = 100 \text{ km s}^{-1}$ , depositing a momentum below the photosphere (the origin) under  $-0^\circ$  angle from the local vertical for the times after shock onset shown above the plots similar to that observed in seismic source 1. The rays are computed numerically for the parameters extracted from the model S (Christensen-Dalsgaard et al. 1996). The rays are colour-coded in the range 9–15 mHz with 9 corresponding to the darkest shade.  $Z$  is depth in the solar interior, the photosphere is denoted by  $Z=0$ , the  $X$ -axis denotes a distance in Mm from the point of the momentum deposition. The mustard arrow shows the direction of the wave propagation. The points of ray reflection from the photosphere seen at 25:17 min in the right top corner are observed as ripples on the surface, or a sunquake, propagating outward the central point of the momentum deposition.

tion of SQ2 where we derived two light curves of white light emission for FE1 and FE2.

For the identification of magnetic field topology and footpoints where all these flaring events can happen we used the NLFFF restoration of the magnetic field and MHD simulations based on the restored magnetic field that helped to obtain the magnetic structure of the active region where flaring events occurred and to link the footpoints of these magnetic ropes to the locations of sunquakes,  $H\alpha$  line kernels, EUV emission with large blue shifts and WL brightening. In practical terms, the area of flaring footpoints were defined from the area of  $H\alpha$  emission kernels or from the area where TD diagrams that allowed to evaluate the initial energy fluxes of particle beams heating these flaring atmospheres using as a basis the parameters derived from the KONUS HXR and GR emission in FE1. For the FE2 we have detected only  $H\alpha$  kernel 3 and white light emission allowing us only speculate about possible conditions of atmosphere heating based on the good fit to the simulated and observed  $H\alpha$  line profiles and light curves of WL emission.

In order to simulate the  $H\alpha$  line profiles for the conditions relevant for the observed kernels we produced the model flaring atmospheres heated by intense mixed beams which were likely present in the flare of 6 September 2017 as per KONUS/WIND

observations with the initial fluxes of  $(6-12) \cdot 10^{12} \text{ erg} \cdot \text{cm}^{-2} \text{ s}^{-1}$  and spectral index of 4, and compared the emission produced in the current hydrodynamic models with those produced in another flare of 6 September 2011 produced by the electron beam with this initial flux of  $4.3 \cdot 10^{11} \text{ erg} \cdot \text{cm}^{-2} \text{ s}^{-1}$ .

These models were used to explain reasonably well the observations of  $H\alpha$  line profiles with CRISP/SST and white light emission from HMI/SDO with the simulated emission of of Balmer line and Paschen continuum, which is seen in white light. These models also helped us to explain upward velocities of the observed EUV spectrograms and their close co-location with the sunquakes 1, 2 and 3 accompanied by the observed dimming and large red-shifts of  $H\alpha$  line emission at the flaring events 1 and 2. We demonstrated with the simulations that WL emission in FE1 and FE2 can only be produced by the same particle beams that produce all other observational signatures, because they induce a strong over-ionisation of hydrogen in the chromosphere and photosphere.

Based on the parameters of the seismic events derived from observations, we apply a combination of two hydrodynamic models: one for a flaring atmosphere heating by a mixed beam and second one for production of acoustic waves in the solar interior by the shock coming from the flaring atmosphere for

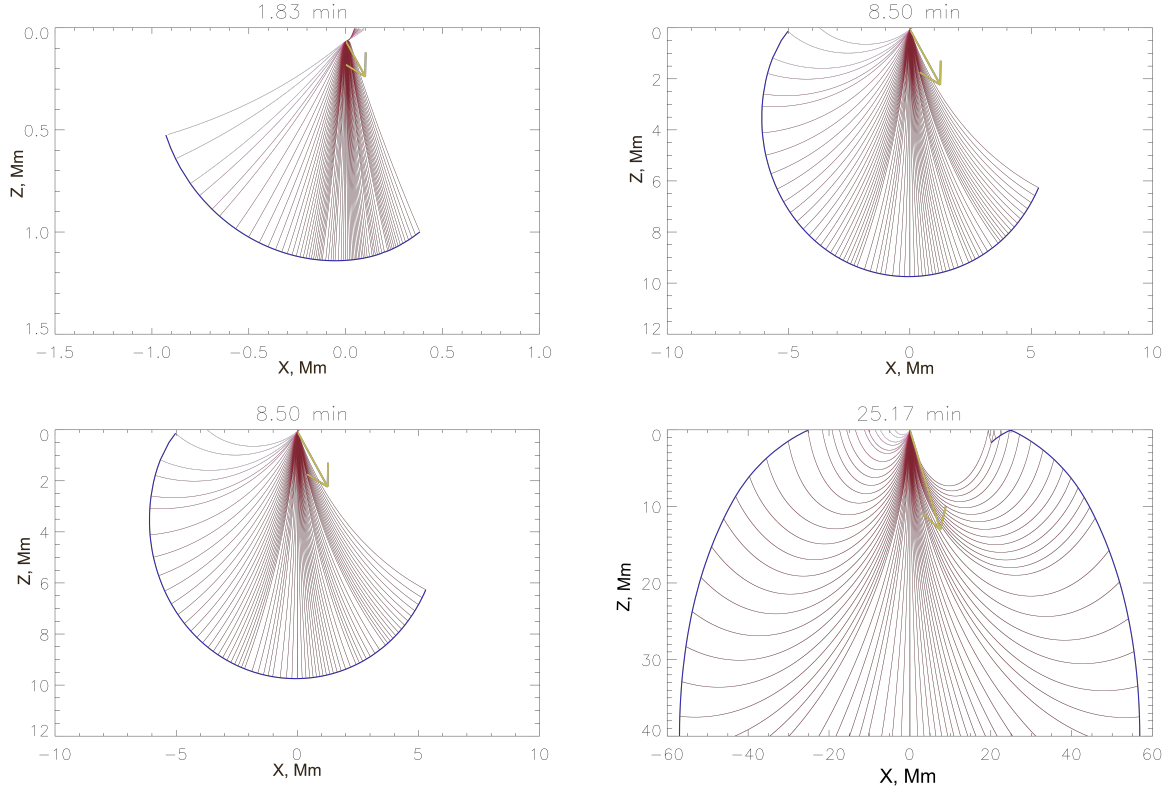


**Fig. 9.** The individual acoustic rays generated at the depth of 45 km in the interior and travelling to the bottom of the plot) by a moving supersonic source with velocity  $v = 150 \text{ km s}^{-1}$ , depositing a momentum below the photosphere under  $+30^\circ$  angle from the local vertical for the times after the shock deposition shown above the plots.  $Z$  is depth in the solar interior, the photosphere is denoted by  $Z=0$ , the  $X$ -axis denotes a distance in Mm from the point of the momentum deposition. The mustard arrow shows the direction of the wave propagation. The points of ray reflection from the photosphere seen after 8:50 min in the left top corner are observed as ripples on the surface, or a sunquake, propagating outward the central point of the momentum deposition.

three seismic sources 1, 2 and 3. in order to demonstrate a role of the magnitude and deposition angle of the shock as well as a depth of the shock deposition in the solar interior on the resulting seismic signatures. These models provide the plausible quantitative interpretation of the seismic signatures associated with the hydrodynamic shocks caused by mixed and electron beam injection in flaring events of this flare.

The simulations show that the explosive evaporation of the plasma heated by a mixed beam starts from the very first seconds with high macrovelocities of  $100 \text{ km s}^{-1}$  similar to that simulated in the lower flaring corona (Fig. 2c, left column), and approaching the velocities of  $400\text{--}500 \text{ km s}^{-1}$  at 5 seconds after the beam onset, which later are reduced to  $250 \text{ km/s}$  at 30–50 s after the event onset. However, observations by Fe XXIII line only started 10–15 seconds after the beam onset, when the beam was off after 10 second and plasma was cooled off to the temperature of few millions K required to see this emission. The spectrograms of the Fe XXIII  $263.76 \text{ \AA}$  line for the FE1 in the footpoint FP3 of SQ 1 reveal large upward velocities of  $300\text{--}350 \text{ km s}^{-1}$ , similar to the simulated velocities in the hydrodynamic model of flaring atmosphere heated by the mixed beam. For SQ2 the blue shift in the line of Fe XXIII  $263.76 \text{ \AA}$ , indicating the macro-velocity of explosive evaporation exceeds  $400 \text{ km/s}$  much faster than in the atmosphere with SQ1 that indicates a stronger shock in the location of SQ2, which was

likely to lead to the additional ridge in time distance diagram of sunquake 2 constituting a double bounce of acoustic waves.

These upward motions are combined with the downflows of  $> 100\text{--}200 \text{ km s}^{-1}$  seen in the He II spectrograms associated with SQ 1 and SQ2. However, the EIS observations in He II  $256 \text{ \AA}$  in the locations of SQ1 and SQ 2 appear 30 s after the onset of FE1 confirming that the temperature of flaring atmosphere reached the magnitudes of radiative temperature of He II line. To this point also indicate the starting time of the SQ1 and SQ2, which is 20–25 s earlier than the red shift in He II line. Although, the red shift in He II line exists for about a minute that is close to that predicted by hydrodynamic simulations. What is remarkable that after a minute or so these downflows are followed by upflows with the magnitudes of macrovelocities close to those predicted by the hydrodynamic (HD) simulations carried out for heating by a mixed beam (in SQ 1 and SQ 2).

It can be observed that the upwards macrovelocities in the HD model approach  $300\text{--}400 \text{ km/s}$ , similar to those measured by the EIS instrument for the location of seismic source 1. At the same time, the downward motion modelled for this event also reaches the macrovelocity of  $300 \text{ km/s}$  at 5 seconds after the beam onset and then is reduced to  $150\text{--}200 \text{ km/s}$  for the next few minutes. These red shifts are close to that measured in H $\alpha$  kernel 1 which was likely to be red-shifted by  $3\text{--}4 \text{ \AA}$ , so only the

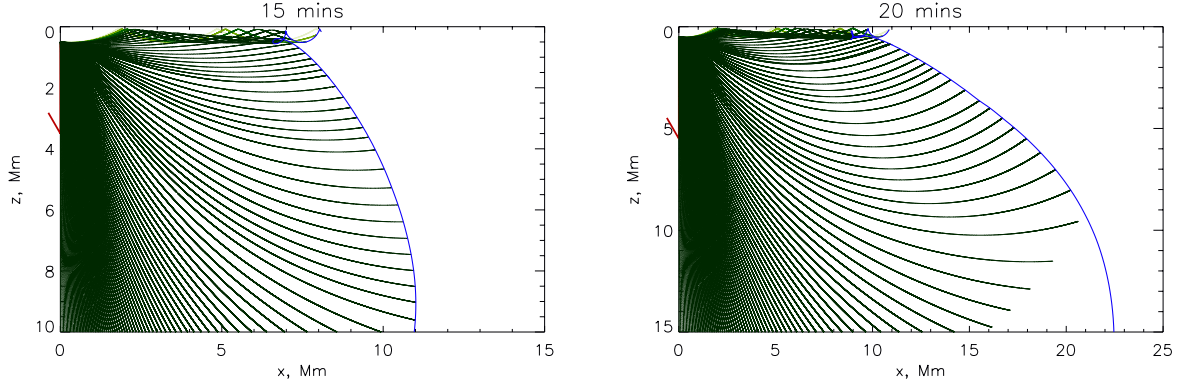


**Fig. 10.** The individual acoustic rays travelling to the bottom of the plot generated in the interior by a moving supersonic source with average speed of  $v = 175 \text{ km s}^{-1}$  like in the seismic source 2 at the times denoted on the top. The shock is inclined by  $-30^\circ$  to the local vertical.  $Z$  is depth in the solar interior, the photosphere is denoted by  $Z=0$ , the  $X$ -axis denotes a distance in Mm from the point of the momentum deposition. The mustard arrow shows the direction of the wave propagation. The points of reflection from the surface are observed at 15 minutes after the deposition time starting from a distance 2 Mm (on the right) and very well seen in 20 minutes at distance starting from 3-4 Mm. The second bounce waves are appearing at 5 Mm in 15 minutes after the shock deposition and at 7 Mm in 20 minutes (see the the top far end of the wave set marked by the blue curve). Note, a video animation of these acoustic waves is presented in the supplementary materials showing propagation of the generated acoustic waves with the first and second bounces as observed in seismic source 2.

blue wing of the line has been observed. At the same time, the He II 256 Å spectrograms in the location of a largest sunquake 2 reveal that similarly to the hydrodynamic simulations the red-shifts approaching  $380 \text{ km s}^{-1}$  dropping to  $250\text{--}300 \text{ km/s}$  15-20 seconds after the beam offset. The observed He II red-shifts in excess of  $250 \text{ km s}^{-1}$  are well-correlated with those observed in the locations of the largest sunquake 2. This red shift also corresponds to the strong one of 5-6 Å measured in  $H\alpha$  kernel 2, where only the far blue wing is observed with the intensity lower than that in  $H\alpha$  kernel 1. The simulated and measured blue shifts in SQ2 and Fe XXIII line start from  $150 \text{ km/s}$  at 1 second approaching  $400 \text{ km/s}$  within a short timescale of 15-30 seconds.

We also investigate the scenario of acoustic wave generation by hydrodynamic shocks propagating for up 50-60 seconds in the solar interior with supersonic velocities and generating acoustic waves above the acoustic cutoff frequency. During the flare of 6 September 2017 the shocks in the SQs 1-3 were deposited beneath the solar surface and travelled much longer in the interior producing acoustic waves compared to the shock generated in the flare of 6 September 2011 reported earlier (Macrae et al. 2018). This difference in the shock deposition depths explain the clear ridges observed in the time-distance diagrams of SQ1, SQ2 and SQ3 in the 6 September 2017 flare versus the rather weak ridge observed in the 2011 flare.

The acoustic waves (rays) generated by the HD shock induced by a mixed beam (MB) in the largest sunquake (source 2) are found to travel much faster and to deposit their momentum much deeper in the solar interior producing acoustic waves of type 1 with the double ridges: a very visible main ridge and a detectable second-bounce ridge. The shocks deposited by an electron beam (EB) produce acoustic waves of type 2 with a weaker single ridge as seen in the seismic sources 1 and 3. As a result, these acoustic waves of type 1 reach the first lower turning point in deeper interior depths, thus, gaining higher velocities compared to the waves of type 2. These type 1 acoustic

waves approach higher velocities in the interior, with which they travel back to the surface in the photosphere to their first upper turning point (or first bounce) creating ripples while being reflected back to the interior. The reflected wave energy is lower than the original one but sufficient to travel again to the less deep interior and to return back for a second bounce creating secondary, slower, ripples.

The acoustic waves of type 1 simulated in the seismic source 2 for a momentum deposited at an angle of  $-30^\circ$  from the vertical and travels rather deep into the solar interior demonstrate the occurrence of strong acoustic waves in the interior. These waves become reflected from the solar surface during the first bounce (or turning point), thus, forming well detectable ripples at the photosphere a few minutes after the impact at a distance approaching 5-10 Mm from the source that is in a close agreement with the distance and time derived from the TD diagram. There are also the second bounce acoustic waves seen in the simulated wave packets occurring at the second upper turning point at the photosphere showing them to start at 5 Mm in the model set at 15 minutes and at 7 Mm in the model set at 20 minutes that is also close to the parameters derived from the TD diagram for seismic source 2.

The other two sources show the acoustic waves, whose characteristics are consistent with those being produced by shocks generated by slightly weaker mixed beams and deposited at angles of  $0^\circ$  (seismic sources 1) and  $+30^\circ$  (source 3) to the local vertical, which propagate beneath the surface but not too deep into the interior, contrary to type 1 acoustic waves in source 2.

Hence, by combining the two hydrodynamic models: of flaring atmosphere and acoustic wave generation in the solar interior, we are able to provide the simultaneous quantitative interpretation of the three seismic events whose characteristics were also confirmed with blue and red shifts derived from the combined with EUV and  $H\alpha$  emission observed in the X9.3 flare of 6 September 2017. We show that in spite of disparity of

spatial and temporal resolution, all the observed signatures can be logically accounted for by the complex hydrodynamic dynamic processes in the flaring atmospheres of interacting magnetic loops and the interior beneath caused by the injection of mixed beams.

## References

- Allred, J. C., Hawley, S. L., Abbett, W. P., & Carlsson, M. 2005, *ApJ*, 630, 573
- Antonucci, E., Gabriel, A. H., Acton, L. W., et al. 1982, *Sol. Phys.*, 78, 107
- Aptekar, R. L., Frederiks, D. D., Golenetskii, S. V., et al. 1995, *Space Sci. Rev.*, 71, 265
- Bradshaw, S. J. & Cargill, P. J. 2006, *A&A*, 458, 987
- Brown, J. C. 1971, *Sol. Phys.*, 18, 489
- Buitrago-Casas, J., Martínez-Oliveros, J., Lindsey, C., et al. 2015, *solphys*, 290, 3151
- Canfield, R. C. & Gayley, K. G. 1987, *ApJ*, 322, 999
- Christensen-Dalsgaard, J., Dappen, W., Ajukov, S. V., et al. 1996, *Science*, 272, 1286
- Cox, D. P. & Tucker, W. H. 1969, *ApJ*, 157, 1157
- Culhane, J. L., Harra, L. K., James, A. M., et al. 2007, *Sol. Phys.*, 243, 19
- Ding, M. D. & Fang, C. 1996, *Sol. Phys.*, 166, 437
- Dominique, M., Hochedez, J.-F., Schmutz, W., et al. 2013, *Sol. Phys.*, 286, 21
- Donea, A. 2011, *Space Sci. Rev.*, 158, 451
- Donea, A. & Lindsey, C. 2005, *ApJ*, 630, 1168
- Donea, A.-C., Besliu-Ionescu, D., Cally, P. S., Lindsey, C., & Zharkova, V. V. 2006, *Solar Physics*, 239, 113
- Donea, A.-C., Braun, D. C., & Lindsey, C. 1999, *ApJ*, 513, L143
- Donea, A.-C., Lindsey, C., & Braun, D. C. 2000, *Sol. Phys.*, 192, 321
- Doschek, G. A., Kreplin, R. W., & Feldman, U. 1979, *ApJ*, 233, L157
- Doschek, G. A., McKenzie, D. E., & Warren, H. P. 2014, *ApJ*, 788, 26
- Druett, M., Scullion, E., Zharkova, V., et al. 2017, *Nature Communications*, 8, 15905
- Druett, M. K. & Zharkova, V. V. 2018, *A&A*, 610, A68
- Druett, M. K. & Zharkova, V. V. 2019, *A&A*, 623, A20
- Duijveman, A., Somov, B. V., & Spektor, A. R. 1983, *Sol. Phys.*, 88, 257
- Fisher, G. H., Bercik, D. J., Welsch, B. T., & Hudson, H. S. 2012, *Sol. Phys.*, 277, 59
- Fisher, G. H., Canfield, R. C., & McClymont, A. N. 1985a, *ApJ*, 289, 434
- Fisher, G. H., Canfield, R. C., & McClymont, A. N. 1985b, *ApJ*, 289, 425
- Fisher, G. H., Canfield, R. C., & McClymont, A. N. 1985c, *ApJ*, 289, 425
- Fisher, G. H., Canfield, R. C., & McClymont, A. N. 1985d, *ApJ*, 289, 414
- Fisher, G. H., Canfield, R. C., & McClymont, A. N. 1985e, *ApJ*, 289, 414
- Gordovskyy, M., Zharkova, V. V., Voitenko, Y. M., & Goossens, M. 2005, *Advances in Space Research*, 35, 1743
- Green, L. M., Valori, G., Zuccarello, F. P., et al. 2017, *ApJ*, 849, 40
- Hochedez, J.-F., Schmutz, W., Stockman, Y., et al. 2006, *Advances in Space Research*, 37, 303
- Hudson, H., Fisher, G., & Welsch, B. 2008, in *Astronomical Society of the Pacific Conference Series*, Vol. 383, *Subsurface and Atmospheric Influences on Solar Activity*, ed. R. Howe, R. Komm, K. Balasubramaniam, & G. Petrie, 221
- Ichimoto, K. & Kurokawa, H. 1984, *Sol. Phys.*, 93, 105
- Inoue, S., Shiota, D., Bamba, Y., & Park, S.-H. 2018, *ApJ*, 867, 83
- Ivanov, V. V. & Serbin, V. M. 1984, *Soviet Ast.*, 28, 405
- Kaempfer, N. & Magun, A. 1983, *ApJ*, 274, 910
- Kennedy, M. B., Milligan, R. O., Allred, J. C., Mathioudakis, M., & Keenan, F. P. 2015, *A&A*, 578, A72
- Kobylinskii, V. A. & Zharkova, V. V. 1996, *Advances in Space Research*, 17, 129
- Kosovichev, A. 2011, *arXiv preprint arXiv:1103.1707*
- Kosovichev, A. G. & Zharkova, V. V. 1998, *Nature*, 393, 317
- Kotrč, P., Procházka, O., & Heinzel, P. 2016, *Sol. Phys.*, 291, 779
- Kuridze, D., Mathioudakis, M., Simões, P. J. A., et al. 2015, *ApJ*, 813, 125
- Kurokawa, H., Takakura, T., & Ohki, K. 1988, *PASJ*, 40, 357
- Lemen, J. R., Title, A. M., Akin, D. J., et al. 2011, *Sol. Phys.*, 241
- Lin, R. P., Dennis, B. R., Hurford, G. J., et al. 2002, *Sol. Phys.*, 210, 3
- Lindsey, C. & Braun, D. 2000, *solphys*, 192, 261
- Lindsey, C. & Braun, D. C. 1999, *ApJ*, 510, 494
- Liu, C., Deng, N., Lee, J., et al. 2014, *Apj*, 795, 128
- Lysenko, A. L., Anfinogentov, S. A., Svinkin, D. S., Frederiks, D. D., & Fleishman, G. D. 2019, *ApJ*, 877, 145
- Macrae, C., Zharkov, S., Zharkova, V., et al. 2018, *A&A*, 619, A65
- Martínez-Oliveros, J.-C., Hudson, H. S., Hurford, G. J., et al. 2012, *ApJ*, 753, L26
- Matthews, S. A., Harra, L. K., Zharkov, S., & Green, L. M. 2015, *ApJ*, 812, 35
- Matthews, S. A., Zharkov, S., & Zharkova, V. V. 2011, *ApJ*, 739, 71
- Milligan, R. O. 2015, *Sol. Phys.*, 290, 3399
- Milligan, R. O., Kerr, G. S., Dennis, B. R., et al. 2014, *ApJ*, 793, 70
- Polito, V., Reep, J. W., Reeves, K. K., et al. 2016, *ApJ*, 816, 89
- Quinn, S., Reid, A., Mathioudakis, M., et al. 2019, *ApJ*, 881, 82
- Radziszewski, K., Rudawy, P., & Phillips, K. J. H. 2011, *A&A*, 535, A123
- Romano, P., Elmhamdi, A., Falco, M., et al. 2018, *ApJ*, 852, L10
- Scharmer, G. B. 2006, *A&A*, 447, 1111
- Scharmer, G. B., Dettori, P. M., Lofdahl, M. G., & Shand, M. 2003, in *Society of Photo-Optical Instrumentation Engineers (SPIE) Conference Series*, Vol. 4853, *Innovative Telescopes*

- and Instrumentation for Solar Astrophysics, ed. S. L. Keil & S. V. Avakyan, 370–380
- Scherrer, P. H., Schou, J., Bush, R. I., et al. 2012, *Sol. Phys.*, 275, 207
- Sharykin, I. N. & Kosovichev, A. G. 2018, *ApJ*, 864, 86
- Shelyag, S., Zharkov, S., Fedun, V., Erdélyi, R., & Thompson, M. J. 2009, *A&A*, 501, 735
- Shmeleva, O. P. & Syrovatskii, S. I. 1973, *Sol. Phys.*, 33, 341
- Siversky, T. V. & Zharkova, V. V. 2009, *Journal of Plasma Physics*, 75, 619
- Somov, B. V., Spektor, A. R., & Syrovatskii, S. I. 1981, *Sol. Phys.*, 73, 145
- Syrovatskii, S. I. & Shmeleva, O. P. 1972, *Soviet Astronomy*, 16, 273
- Uchida, Y. & Hudson, H. 1972, *Sol. Phys.*, 26, 414
- Veronig, A., Vršnak, B., Temmer, M., & Hanslmeier, A. 2002, *Sol. Phys.*, 208, 297
- Woods, T. N., Lean, J. L., & Eparvier, F. G. 2006, in *Proceedings of the ILWS Workshop*, ed. N. Gopalswamy & A. Bhattacharyya, 145
- Wuelser, J.-P. & Marti, H. 1989, *ApJ*, 341, 1088
- Zarro, D. M., Canfield, R. C., Metcalf, T. R., & Strong, K. T. 1988, *ApJ*, 324, 582
- Zhao, J. & Chen, R. 2018, *ApJ*, 860, L29
- Zharkov, S. 2013, *Monthly Notices of the Royal Astronomical Society*, 431, 3414
- Zharkov, S., Green, L., Matthews, S., & Zharkova, V. 2011b, *ApJ*, 741, L35
- Zharkov, S., Matthews, S., Zharkova, V., et al. 2020, , in press, Paper 1
- Zharkov, S., Zharkova, V. V., & Matthews, S. A. 2011a, *ApJ*, 739, 70
- Zharkova, V. & Kobylinskii, V. 1993, *Sol. Phys.*, 143, 259
- Zharkova, V. & Zharkov, S. 2007, *ApJ*, 664, 573
- Zharkova, V. & Zharkov, S. 2015, *Sol. Phys.*, 290, 3163
- Zharkova, V. V. 2008, *Sol. Phys.*, 251, 641
- Zharkova, V. V., Arzner, K., Benz, A. O., et al. 2011, *Space Sci. Rev.*, 159, 357
- Zharkova, V. V. & Gordovskyy, M. 2006, *ApJ*, 651, 553
- Zharkova, V. V. & Kobylinskii, V. A. 1993, *Sol. Phys.*, 143, 259
- Royal Observatory of Belgium, funded by the Belgian Federal Science Policy Office (BELSPO) and by the Swiss Bundesamt fuer Bildung und Wissenschaft. M. Druett’s acknowledges the support of his research by the Swedish Research Council, grant number 2017-04099. S. Zharkov and V. Zharkova acknowledge the funding for this research provided by the U.S. Air Force grant PRJ02156. S. Matthews acknowledges a financial support from STFC via the Consolidated Grant ST/N000722/1.

## 6. Acknowledgements

The authors wish to express their deep gratitude to the anonymous referee for constructive and useful comments, from which the paper strongly benefited. The authors express their gratitude to Dr. A. Lysenko (IOFFE Institution, St. Petersburg, Russia) for offering the KONUS data with their full explanations and useful discussion. The authors acknowledge that HMI and AIA images are available by courtesy of NASA/SDO and the AIA, EVE, and HMI science teams. The Swedish 1-m Solar Telescope is operated on the island of La Palma by the Institute for Solar Physics of Stockholm University in the Spanish Observatorio del Roque de los Muchachos of the Instituto de Astrofísica de Canarias. The LYRA is a project of the Centre Spatial de Liege, the Physikalisches-Meteorologisches Observatorium Davos, and the